

Growth of lamellar eutectic structures: The axisymmetric state

K. Kassner

Institut für Festkörperforschung des Forschungszentrums Jülich, 517 Jülich, Germany

C. Misbah

Groupe de Physique des Solides, Université Paris VII et Paris VI, place Jussieu, 75005 Paris, France

(Received 20 March 1991)

We study steady symmetric lamellar eutectic growth in directional solidification by an extensive analysis of the pertinent boundary integral equation. We find a discrete set of solutions that differ in their average undercoolings. As the wavelength λ increases, the branches coalesce by pairs to form fold singularities above which axisymmetric solutions cease to exist. Front shapes are computed in a wide range of wavelengths, and a systematic comparison with an improved Jackson and Hunt theory [Trans. Metall. Soc. AIME **236**, 1129 (1966)] is made. The last one turns out to be accurate in general, for the lowest branch, but does not provide any hint at other branches. In the experimentally relevant parameter range, the front equation reduces to a similarity equation containing two dimensionless parameters $\sigma \equiv d_0 l / \lambda^2$ and $\chi \equiv l / l_T$, where d_0, l, l_T are the capillary, diffusion, and thermal lengths. We explicitly demonstrate the similarity properties of the pattern. The selected wavelength scales as $\lambda \approx \sqrt{d_0 l f(l/l_T)}$. At the minimum undercooling, λ varies with the growth velocity V as $V^{-\beta}$, where β is an increasing function of V that saturates to about $\frac{1}{2}$ at large V . This feature is in agreement with experiments [G. Lesoult, Ann. Chim. Fr. **5**, 154 (1980)]. The general scaling of the wavelength allows the exact prediction of a new scaling exponent that is independent of the nature of the selection criterion. This prediction inspires another experimental test of the theory.

PACS number(s): 61.50.Cj, 05.70.Fh, 81.30.Fb, 68.70.+w

I. INTRODUCTION

Most solidification microstructures can be broadly classified into two important growth morphologies: dendritic and eutectic microstructures. It is therefore not surprising that particularly these morphologies give rise to intensive investigations both experimentally and theoretically. The issue that has seen considerable progress to date is the velocity selection dilemma of a free dendrite [1].

Another issue is that of pattern formation in directional solidification of thin-film alloys, which reveals fascinating spatially organized patterns. The basic features of the system are shown in Fig. 1. The sample consists of a thin strip of the working material, which is pushed, at a predetermined velocity V , through a fixed temperature gradient G established by stationary hot and cold contacts A and B . The most common liquid-solid equilibrium phase diagram is the one displayed in Fig. 2. If the concentration of the major phase is very small (a dilute alloy), one often observes the growth of one solid phase (the major one) at the expense of its melt. It is by now well established that such a situation leads to the Mullins-Sekerka [2] instability of the planar front above a critical velocity; the interface turns into a parallel array of cellular shapes, which bifurcate into dendrites at larger speeds [3], not talking about other fascinating structures, among them solitary modes [4]. The other situation, in which we are interested here, is the one where the composition is close to the eutectic one [5] (Fig. 2). The growing solid often forms a parallel array of the two

coexisting phases α and β that grow side by side. This is the lamellar eutectic growth [6,7].

The growth of lamellar eutectics has been the subject of several theoretical investigations. Perhaps the best known work is that of Jackson and Hunt (JH) [8]. Their basic idea is the replacement of the diffusion field in the liquid phase by that of a planar front. They further assume that the two lamellae α and β have equal average undercoolings. Trivedi, Mason, and Kurz [9] extended the work of JH by using a more detailed form of the diffusive Green's function that is valid at large velocities. The justification of the flat interface assumption of JH remained open, however. More recently, Brattkus, Caroli, Caroli, and Roulet [10] have discussed that issue. It emerged from their analysis that the JH approximation is

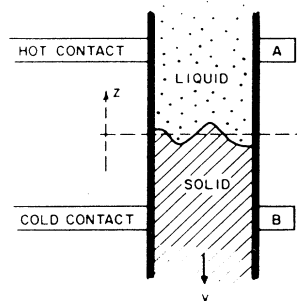


FIG. 1. Schematic setup of a directional solidification experiment.

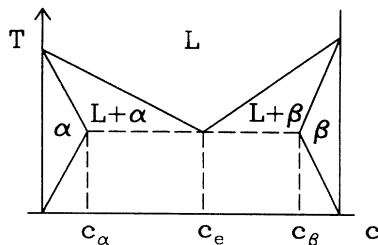


FIG. 2. Generic phase diagram of eutectics. T is the temperature, c the concentration of one component. The regions L , α , and β correspond to one-phase equilibrium states of the liquid, the solid α , and the solid β phases, respectively. $L + \alpha$ and $L + \beta$ are regions of two-phase equilibrium between the liquid and one solid phase; the actual concentrations of the two phases are given by the liquidus and solidus lines (full lines) delimiting these regions. c_e , c_α , and c_β denote the equilibrium concentrations of the liquid and the two solid phases at the triple or eutectic point.

justified only for large thermal gradients, that is when $l_T/l \ll 1$, where l and l_T are the diffusion and thermal lengths, respectively (for their precise definition, see Sec. II). They further showed that the assumption of equal undercoolings of both phases is unnecessary but does not alter the qualitative features found by JH.

Most of the experiments, however, operate at thermal gradients such that $l_T/l \approx O(1)$. We should therefore deal with a complete solution of the growth equations. The main objective of this paper is to present an extensive study of steady lamellar eutectics. This is done by numerically integrating the boundary integral equation. We have made a systematic calculation of stationary symmetric front profiles. Our code accounts for arbitrary phase diagrams. This means, in particular, that the volume fraction of each solid phase (α and β) is not fixed *a priori* (as is the case if one assumes a vanishing solid solubility) but adjusted self-consistently in the diffusion field. Another feature is that the JH assumption of equal undercoolings for the two phases α and β appears, in a very natural way, as unnecessary when counting the number of unknowns and that of equations. In other words, the eutectic problem is closed and does not require any additional assumption.

The main lines of this work can be summarized as follows.

(i) We have made a comprehensive comparison of our results with those obtained from a JH-type theory. First we compute the shapes and the associated average undercoolings for a wide range of wavelengths. The average undercooling takes on a minimum but the average undercoolings of the α and β phases are appreciably different. As the wavelength λ increases above the one that provides the minimum undercooling, the interface exhibits tip-splitting modes and starts to form “pockets” on further increase of λ . However, before these can develop fully (in the lowest solution branch) the axisymmetric solution to the growth equations ceases to exist by running into a fold singularity. There *are* solutions beyond the fold, but these are not axisymmetric. They are the

tilted states found recently [11], and we plan to devote a separate publication to their discussion.

(ii) We compare the exact shapes of axisymmetric solutions to those obtained from an improved JH theory, which is constructed by inserting the JH diffusion field into the Gibbs-Thomson equation and solving numerically the resulting nonlinear differential equation. Surprisingly enough, an improved JH theory provides profiles that are accurate within a few percent even in the standard experimental range where $l_T \approx l$. This theory, however, misses the aforementioned fold singularity; symmetric solutions extend to very large values of the wavelength.

(iii) We demonstrate that the fully nonlinear problem supports a discrete set of solutions. More precisely, for fixed material and control parameters the integral equation possesses solutions with distinguishable shapes having different average undercoolings. This feature as well as the fold singularity have not, to our knowledge, been discussed previously. It is likely that only the solution with the smallest undercooling is stable. This *discrete* degeneracy should not be confused with the *continuous* degeneracy in the JH theory, which pertains to wavelength selection. The present discrete degeneracy appears similar to that encountered in the problem of velocity selection of a free dendrite [1].

(iv) Taking advantage of the fact that in standard experiments the Péclet number $P \equiv \lambda/l$ is small ($P \approx 10^{-2}$), we have recently [12] shown that the full boundary integral equation reduces to a nonlinear similarity equation containing only two dimensionless parameters $\sigma \equiv d_0 l / \lambda^2$, $\chi \equiv l/l_T$, where d_0 is a capillary length. Here we give an extensive derivation of that equation without any restriction (e.g., $l_T^\alpha = l_T^\beta$. . .). We demonstrate the similarity property of the pattern. In particular, we show that the front profile is invariant, up to a scale factor given by the wavelength, under a simultaneous stretching (shrinkage) of λ and (G, V) by α and α^{-2} , respectively, where α is a positive number. We comment on the scaling of the wavelength with the growth velocity V presented recently [12], when the operating point is assumed to be the one that corresponds to the minimum undercooling. The general form of the scaling of the wavelength

$$\lambda \approx \sqrt{d_0 l} f(l/l_T) \quad (1.1)$$

inspires additional experimental tests whatever the selection criterion. In particular, if l/l_T is kept fixed, one expects, according to Eq. (1.1), to find that $\lambda^2 V = \text{const}$. There exist a variety of experiments [13] where $\lambda^2 V$ was observed, as found in our theory for the minimum undercooling [12], to significantly decrease with V at small enough V when the thermal gradient, not l/l_T , was maintained at a fixed value.

The scheme of this paper is as follows. In Sec. II, we write down the growth equations, which are then transformed into a boundary integral equation that governs one-dimensional front deformations. The results emerging from the JH theory are briefly recalled in Sec. III. In Sec. IV, we present the numerical method to solve the front equations. Section V contains the results. Sec-

tion VI is devoted to the derivation of the similarity equations and to the main results that follow from similarity. Section VII concludes and summarizes the paper. Some mathematical details are given in three appendixes.

II. MODEL EQUATIONS

We consider a standard simplification of the physical system, which is believed to capture its essential physical features. In particular, the simplifying assumptions of the model are the following. The thermal gradient G is constant throughout the system. This means that thermal diffusion is much faster than chemical diffusion, that thermal conductivities in all phases are equal, and that latent heat production can be neglected. In addition, to reduce the diffusion problem even further, it is assumed that there is no (chemical) diffusion in the solid phase (one-sided model). This is a good approximation in many cases. As usual (for an exception see Ref. [14]) we assume the attachment kinetics at the solid-liquid interface to be fast on the time scales of all transport problems. This assumption is legitimate for a microscopically rough interface. Furthermore, we "linearize" the phase diagram of the eutectic—see Fig. 2—in assuming constant slopes of the liquidus and solidus lines on both sides of the eutectic point, which results in temperature-independent partition coefficients k_α and k_β . Finally, we restrict ourselves here to the case of isotropic surface tension. Figure 2 may serve to identify some of the quantities needed in the definition of the model equations that are to follow.

Introducing a dimensionless concentration field $u = (c - c_e)/\Delta c$, where c stands for the physical concentration and $\Delta c = c_\beta - c_\alpha$ is the miscibility gap, we can write the equation of motion in the laboratory frame (where the sample is pushed at constant velocity V along the $-z$ direction)

$$\frac{1}{D} \frac{\partial u}{\partial t} = \nabla^2 u + \frac{2}{l} \frac{\partial u}{\partial z}. \quad (2.1)$$

Here $l = 2D/V$ is the diffusion length (D is the diffusion constant).

The diffusion equation (2.1) has to be supplemented by boundary conditions. At infinity, the concentration is kept at a constant value: $u_\infty = (c_\infty - c_e)/\Delta c$. Thermodynamics provides us via the local equilibrium assumption with the Gibbs-Thomson condition:

$$u = \begin{cases} -\xi/l_T^\alpha - d_0^\alpha \kappa, & \alpha \text{ phase} \\ \xi/l_T^\beta + d_0^\beta \kappa, & \beta \text{ phase} \end{cases}. \quad (2.2)$$

In these equations, ξ is the z coordinate of the liquid-solid interface; κ is its curvature, taken positive where the solid is convex. In principle, the model can be formulated in arbitrary dimensions (in three dimensions, κ is the sum of the two principal curvatures). Since we are, however, interested in lamellar structures, we restrict ourselves here to two dimensions or a one-dimensional interface. $l_T^{\alpha/\beta}$ are the thermal lengths, given by $l_T^i = m_i \Delta c / G$, where m_i ($i = \alpha, \beta$) is the absolute value of the slope of the liquidus line describing coexistence of phase i and the liquid. d_0^i

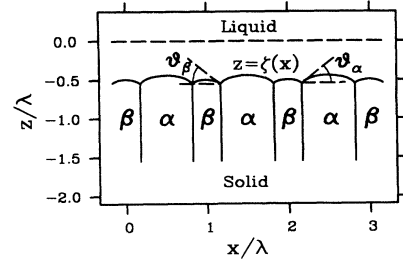


FIG. 3. Illustration of a lamellar eutectic in the comoving coordinate system. The growth direction (in the laboratory frame) is upward, parallel to the z axis. The interface is determined by $z = \zeta(x)$. Also shown are the pinning angles ϑ_α and ϑ_β .

are the capillary lengths, $d_0^i = \gamma_{il} T_e / L_i m_i \Delta c$; γ_{il} is the liquid-solid- i interface tension and L_i is the latent heat per unit volume [15].

Local equilibrium includes mechanical equilibrium at the triple points, which leads to the conditions

$$\begin{aligned} \gamma_{\alpha l} \sin \vartheta_\alpha + \gamma_{\beta l} \sin \vartheta_\beta &= \gamma_{\alpha\beta}, \\ \gamma_{\alpha l} \cos \vartheta_\alpha - \gamma_{\beta l} \cos \vartheta_\beta &= 0, \end{aligned} \quad (2.3)$$

where ϑ_α and ϑ_β are the pinning angles—see Fig. 3.

Owing to mass conservation we obtain a boundary condition for the normal derivatives of the concentration field at the interface. This continuity equation reads

$$-D \frac{\partial u}{\partial n} = \begin{cases} [(1 - k_\alpha)u + \delta] v_n, & \alpha \text{ phase} \\ [(1 - k_\beta)u + \delta - 1] v_n, & \beta \text{ phase} \end{cases} \quad (2.4)$$

where $\delta = (c_e - c_\alpha)/\Delta c$ is the reduced miscibility gap of the α phase and $1 - \delta$ that of the β phase. $v_n = (2D/l + \xi)n_z$ is the normal velocity of the interface; the normal vector points from the solid into the liquid [16].

Equations (2.1)–(2.4) are assumed to refer to a periodic interface with wavelength λ . We may then ask in which way we can arrive at a well-posed mathematical problem using these equations. In general, solving the diffusion equation involves prescribing the values of the diffusing field on the domain of interest at the initial time as well as conditions at its boundaries for all later times. This is clearly not what we are interested in, because we wish to assume that any initial transients have decayed. Throwing away the time derivative of (2.1), we obtain an elliptic problem whose solution requires *just* the field values on the boundaries. This means that (2.1) plus (2.2) and (2.3) have solutions for arbitrary boundary shapes, but of course the normal derivatives will not satisfy (2.4), i.e., the solutions are not physical. The only meaningful question that we can ask, once we have reduced the problem to an elliptic one, is what boundary ξ can we choose such that both (2.2) and (2.4) hold. Hence, the boundary integral formulation for Eqs. (2.1)–(2.4), which we will give immediately, constitutes a functional equation for the interface $\xi(x)$. A derivation of this integral formulation may be found in Ref. [17].

The resulting integro-differential equation condenses the diffusion equation (2.1) and its boundary conditions into a single expression. In the present stationary case it may be written [18]

$$\int_{\Gamma_{st}} d\Gamma' g(\mathbf{r}, \mathbf{r}') \frac{\partial u}{\partial n'} = \int_{\Gamma_{st}} d\Gamma' h(\mathbf{r}, \mathbf{r}') [u(\mathbf{r}') - u_\infty] \quad (2.5)$$

with

$$h(\mathbf{r}, \mathbf{r}') = \left[\frac{\partial g}{\partial n'} - \frac{2}{l} n'_z g(\mathbf{r}, \mathbf{r}') \right] - \frac{1}{2} \delta(\mathbf{r} - \mathbf{r}') . \quad (2.6)$$

The integral can be restricted to the solidification front Γ_{st} , because $u(\mathbf{r}) - u_\infty$ vanishes at infinity—for a more detailed discussion see Ref. [18]. $\mathbf{r} = (x, \zeta(x))$ and \mathbf{r}' are two-dimensional (2D) position vectors of interface points, $\delta(\mathbf{r} - \mathbf{r}')$ is a one-dimensional δ function, and $g(\mathbf{r}, \mathbf{r}')$ is the Green's function associated with the stationary form of Eq. (2.1):

$$g(\mathbf{r}, \mathbf{r}') = \frac{1}{2\pi} e^{-(\zeta - \zeta')/l} K_0(|\mathbf{r} - \mathbf{r}'|/l) , \quad (2.7)$$

wherein K_0 is the modified Bessel function of order zero (Macdonald's function).

For use in Sec. VI below, we find it convenient to cast (2.5) into dimensionless form by measuring lengths in units of λ , i.e., we make the replacements $\mathbf{r} \rightarrow \lambda \mathbf{r}$, $\partial/\partial n' \rightarrow \lambda^{-1} \partial/\partial n'$, $d\Gamma' \rightarrow \lambda d\Gamma'$. This leads to a natural introduction of the Péclet number $P = \lambda/l$ and transforms (2.5) into

$$\begin{aligned} \frac{u}{2} = u_\infty - \frac{P}{2\pi} \int_{-\infty}^{\infty} dx' e^{-P\Delta\zeta} K_0(P\rho) \left[u(\mathbf{r}') + \frac{1}{Pn'_z} \frac{\partial u}{\partial n'} \right] \\ + \frac{P}{2\pi} \int_{-\infty}^{\infty} dx' e^{-P\Delta\zeta} K_1(P\rho) \frac{\Delta\zeta - \Delta x \zeta_{x'}}{\rho} u(\mathbf{r}') . \end{aligned} \quad (2.8)$$

Here, we have introduced the abbreviations $\Delta\zeta = \zeta - \zeta'$, $\Delta x = x - x'$ for (dimensionless) coordinate differences. $\zeta_{x'}$ is shorthand for $d\zeta/dx'$ and $\rho = (\Delta x^2 + \Delta\zeta^2)^{1/2}$. K_1 denotes the modified Bessel function of first order. In deriving (2.8), we have employed the sum rule

$$\int_{\Gamma_{st}} d\Gamma' \left[\frac{\partial g}{\partial n'} - 2Pn'_z g(\mathbf{r}, \mathbf{r}') \right] = -\frac{1}{2} , \quad (2.9)$$

which essentially is known from other sources [17,18], but will be briefly derived in Appendix A for the convenience of the reader.

In order to avoid confusion, we admit right from the start that we will use the same notation for coordinates, throughout the paper, whether they are measured in physical units (as in Sec. III) or reduced by either l_T (Sec. V) or λ (Sec. VI). In each section, the introductory remarks will clarify in which units lengths are given; furthermore, in *figures* we write ζ/λ or x/λ , whenever the coordinates are measured in units of λ .

III. THE JACKSON-HUNT THEORY

A theory for axisymmetric lamellar growth in the steady state was put forward by Jackson and Hunt [8]. The basic idea of their calculation is to replace, at a first level of approximation, the diffusion field by that of a planar lamellar structure sitting at the average position of the actual solidification front. Using this diffusion field in (2.2), those equations transform into ordinary second-order differential equations for the interface position $\zeta(x)$, which can be solved in principle. This is the second stage of approximation. The analysis is greatly simplified by assuming the undercooling of both phases to be equal. However, neither is this assumption well justified as has been pointed out recently [10] nor is it necessary, as we shall see below. When referring to the term *improved JH theory* in the following, we mean a JH-type theory, where the JH diffusion field is inserted in the Gibbs-Thomson equation and the resulting equations are solved numerically without resort to the equal undercooling assumption. In the subsequent brief description of the JH theory, we largely follow the notation of Ref. [19]. Lengths are measured in physical units.

First, we write the general solution of the stationary diffusion equation for a spatially periodic system as

$$u(x, z) = u_\infty + \sum_{n=-\infty}^{\infty} B_n e^{-Q_n(z-\bar{\zeta})} e^{iK_n x} , \quad (3.1)$$

where

$$K_n = \frac{2\pi n}{\lambda} , \quad Q_n = \frac{1}{l} + \left[\frac{1}{l^2} + K_n^2 \right]^{1/2} . \quad (3.2)$$

If the simplifying (unessential) assumption is made that the partition coefficients of both phases are equal, $k_\alpha = k_\beta = k$ ($\neq 0$), one immediately obtains the coefficients B_n by inserting (3.1) into the continuity equation (2.4) and evaluating both sides at $\zeta = \bar{\zeta} = \text{const}$. This procedure yields

$$B_0 = \frac{1}{k} [(1-k)u_\infty + \delta + \eta - 1] , \quad (3.3)$$

where η is the volume fraction of the α phase, and

$$B_n = \frac{4e^{-i\eta K_n \lambda/2} \sin(\eta K_n \lambda/2)}{l\lambda K_n (Q_n - 2/l)} , \quad n \neq 0 . \quad (3.4)$$

In the chosen coordinate system, an α lamella is located in the x interval $[0, \eta\lambda]$. All quantities depend on the yet undetermined value of η . (For $k=0$, η is fixed but B_0 remains indeterminate at this stage [19].) Assuming $\lambda \ll l$, we obtain for the diffusion field

$$\begin{aligned} u(x, z) = u_\infty + \frac{1}{k} [(1-k)u_\infty + \delta + \eta - 1] e^{-2(z-\bar{\zeta})/l} \\ + 2\frac{\lambda}{l} \sum_{n=1}^{\infty} \frac{\sin(n\pi\eta)}{(n\pi)^2} \\ \times \cos \left[2n\pi \left[\frac{x}{\lambda} - \frac{\eta}{2} \right] \right] e^{-2n\pi(z-\bar{\zeta})/\lambda} . \end{aligned} \quad (3.5)$$

Using

$$\kappa = -\frac{\zeta_{xx}}{(1+\zeta_x^2)^{3/2}}, \quad (3.6)$$

we obtain from (2.2)

$$d_0^i \frac{\zeta_{xx}}{(1+\zeta_x^2)^{3/2}} - \frac{\zeta}{l_T^i} = \epsilon_i u(x, \zeta(x)), \quad i = \alpha, \beta \quad (3.7)$$

where $\epsilon_\alpha = 1$, $\epsilon_\beta = -1$. These are two second-order differential equations, whose solutions depend on four integration constants plus the two parameters η and $\bar{\zeta}$, i.e., we have six unknowns. By virtue of (2.3) we have four boundary conditions on the slopes ζ_x at the triple points. Furthermore, we obtain one equation from the requirement that the solutions in the α and β phases have to join continuously at the triple points—this is only one condition (and not two) because of the symmetry of the pattern with respect to the central axis of either phase. Finally, we have a self-consistency relation as the sixth equation; the average of $\zeta(x)$ over one periodicity length must be equal to $\bar{\zeta}$,

$$\bar{\zeta} = \langle \zeta(x) \rangle = \eta \langle \zeta \rangle_\alpha + (1-\eta) \langle \zeta \rangle_\beta. \quad (3.8)$$

Hence (given the wavelength) the problem is completely determined, and were it not for the complexity of the nonlinear differential equations (3.7), which prevents their exact analytic solution, there would be no need for an equal undercooling assumption. Numerically, these equations are easily solved and they will be the basis for our comparison of the complete theory with the JH one.

Let us now briefly review the analytic simplifications introduced by JH. The averages of $u(x, \bar{\zeta})$ and κ in the α and β phases are (see, e.g., Ref. [19])

$$\langle u \rangle_\alpha = \frac{1}{k} (u_\infty + \delta + \eta - 1) + \frac{2\lambda}{\eta l} P(\eta), \quad (3.9)$$

$$\langle u \rangle_\beta = \frac{1}{k} (u_\infty + \delta + \eta - 1) - \frac{2\lambda}{(1-\eta)l} P(\eta), \quad (3.10)$$

$$\langle \kappa \rangle_\alpha = \frac{2}{\eta \lambda} \sin \vartheta_\alpha, \quad (3.11)$$

$$\langle \kappa \rangle_\beta = \frac{2}{(1-\eta)\lambda} \sin \vartheta_\beta, \quad (3.12)$$

where

$$P(\eta) = \sum_{n=1}^{\infty} \frac{\sin^2(n\pi\eta)}{(n\pi)^3}. \quad (3.13)$$

Equations (3.11) and (3.12) are exact relations, a consequence only of the definition of curvature and not dependent on the JH theory. With (2.2) we find

$$\langle \zeta \rangle_\alpha = -l_T^\alpha \left[\frac{1}{k} (u_\infty + \delta + \eta - 1) + \frac{2\lambda}{\eta l} P(\eta) \right] - \frac{2l_T^\alpha d_0^\alpha \sin \vartheta_\alpha}{\eta \lambda}, \quad (3.14)$$

$$\langle \zeta \rangle_\beta = l_T^\beta \left[\frac{1}{k} (u_\infty + \delta + \eta - 1) - \frac{2\lambda}{(1-\eta)l} P(\eta) \right] - \frac{2l_T^\beta d_0^\beta \sin \vartheta_\beta}{(1-\eta)\lambda}. \quad (3.15)$$

The assumption that the average undercoolings in front of both phases are equal is the same as setting $\langle \zeta \rangle_\alpha = \langle \zeta \rangle_\beta$, because $\Delta T = -G\zeta$. This yields an equation which in principle determines the volume fraction η (though it is never used in practice),

$$u_\infty + \delta + \eta - 1 = \frac{k}{(l_T^\alpha + l_T^\beta)\eta(1-\eta)} \times \left[\frac{2\lambda}{l} P(\eta) [\eta l_T^\beta - (1-\eta)l_T^\alpha] + \frac{2}{\lambda} [\eta l_T^\beta d_0^\beta \sin \vartheta_\beta - (1-\eta)l_T^\alpha d_0^\alpha \sin \vartheta_\alpha] \right], \quad (3.16)$$

plus, on inserting this back into one of the equations (3.14) or (3.15), produces the famous result for the undercooling

$$\langle \Delta T(\lambda) \rangle = \frac{1}{2} \langle \Delta T \rangle_{\min} \left[\frac{\lambda}{\lambda_{\min}} + \frac{\lambda_{\min}}{\lambda} \right], \quad (3.17)$$

where

$$\lambda_{\min}^2 = [d_0^\alpha (1-\eta) \sin \vartheta_\alpha + d_0^\beta \eta \sin \vartheta_\beta] \frac{l}{P(\eta)}, \quad (3.18)$$

$$\langle \Delta T \rangle_{\min} = \frac{4G}{\eta(1-\eta)} \frac{l_T^\alpha l_T^\beta}{l_T^\alpha + l_T^\beta} \left[\frac{P(\eta)}{l} \right]^{1/2} \times [d_0^\alpha (1-\eta) \sin \vartheta_\alpha + d_0^\beta \eta \sin \vartheta_\beta]^{1/2}. \quad (3.19)$$

Two remarks are in order. First, the wavelength at minimum undercooling behaves as $\lambda \propto V^{-1/2}$ (because $l \propto V^{-1}$, whereas the V dependence of η is negligible) and the minimum undercooling scales as $\langle \Delta T \rangle_{\min} \propto V^{1/2}$. The hypothesis that the operating point of the growing eutectic is determined by the minimum undercooling leads, within the JH theory, to the result that the selected wavelength and the average undercooling should scale as $V^{-1/2}$ and $V^{1/2}$, respectively. Second, the equal undercooling assumption is not the only possible way to analytically simplify the equations. Equally well one could require $\eta = 1 - u_\infty - \delta$ (for $k \neq 0$) or $B_0 = -u_\infty$ (for $k = 0$), which would yield the same scaling relations for the separate phases. This different hypothesis would be motivated by the fact that in experiments the Péclet number is small and that from global mass conservation we have $u_\infty + \delta + \eta - 1 \simeq O(P)$ (which is proved in Appendix B). We will not pursue this possibility further; the only purpose of this comment was to point out that there are other, possibly more legitimate, *ad hoc* assumptions than the equality of the average undercoolings of the two lamellae.

IV. NUMERICAL METHOD

All numerical approaches to the solution of continuous equations consist of two basic steps: discretization of the continuous problem and solution of the ensuing set of discrete equations. As to the present case, the art that is

involved lies completely in the first step since for the second we use a standard iterative nonlinear equation solver, a NAG routine that realizes a Newton-Raphson method.

We start by reducing the parameter space through introduction of dimensionless units expressible via the ratios λ/l (P), d_0/λ , l_T/λ . The time and length scales of

the physical system are set by the diffusion constant (which is set equal to 1 in the numerics) and the thermal length (more details will be given in the following section). Next we exploit the periodicity and axial symmetry of the problem to cut the integration contour down to a half-period. The integral equation (2.5) becomes, in normalized units ($\lambda=1$),

$$\int_{x'=0}^{1/2} d\Gamma' \sum_{m=-\infty}^{\infty} [g(x, \xi; x'+m, \xi') + g(x, \xi; -x'+m, \xi')] \frac{\partial}{\partial n'} u(x', \xi')$$

$$= \int_{x'=0}^{1/2} d\Gamma' \sum_{m=-\infty}^{\infty} [h(x, \xi; x'+m, \xi') + h(x, \xi; -x'+m, \xi')] [u(x', \xi') - u_{\infty}]. \quad (4.1)$$

For technical reasons, we have to restrict the summation on m to a finite number of terms. Because g and h decay exponentially on the length scale of the diffusion length, we take into account only those terms of the sum for which $|x \pm x' \pm m|$ does not exceed ten diffusion lengths plus one wavelength. In addition, the integrand is set equal to zero whenever $|r-r'|$ exceeds ten diffusion lengths.

We discretize the liquid-solid interface by N points. Because we wish to eventually solve for the interface position, it is worthwhile keeping the number of variables needed for its description small by not using the $2N$ Cartesian coordinates, but a set of hybrid variables, allowing a description of the interface by N variables. Figure 4 shows how it works. The internal representation of the interface within one half-period is by the coordinates of the eutectic or triple point (x_e, ξ_e) plus the angles ϑ_i between the z axis and the normal vectors on the discretization intervals. We are thus switching from a Cartesian representation of the interface curve to a representation in terms of the arclength s and the angle $\vartheta(s)$. The arc length itself need not be stored, if we choose all discretization intervals within one phase to have the same length. Given the angles ϑ_i , the arc-length increments Δs_{α} , Δs_{β} are determined by (see Fig. 4)

$$x_1 - x_e = \Delta s_{\beta} \sum_{i=1}^{N_{\beta}-1} \cos \vartheta_i,$$

$$x_e - x_N = \Delta s_{\alpha} \sum_{i=N_{\beta}}^{N_{\alpha}+N_{\beta}-2} \cos \vartheta_i, \quad (4.2)$$

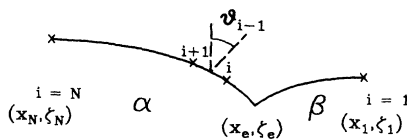


FIG. 4. Discretization elements of the interface. Only the points of one half-period are stored internally. For the discretization procedure and the meaning of the variables see text. Note that the angle belonging to the interval between points i and $i+1$ is ϑ_i in the β phase and ϑ_{i-1} in the α phase.

respectively, N_{α} and N_{β} being the number of discretization points in each phase (the eutectic point is counted twice). Up to an arbitrary translation, x_1 and x_N are fixed by the wavelength (in reduced units, $x_1 - x_N = \frac{1}{2}$), therefore the interface is completely determined by the set of $N_{\alpha} + N_{\beta} = N$ variables $\{x_e, \xi_e, \vartheta_1, \dots, \vartheta_{N-2}\}$.

Obviously, we must calculate the curvature from the N discretization points. For interior points of the sequences $1 \dots N_{\beta}$ and $N_{\beta} + 1 \dots N$ this is easy—we just take three consecutive points and construct the unique circle through them. For the curvatures at the triple point and at the half-cell boundaries we have to use a more sophisticated method. Remembering that a circle is also uniquely determined by two points and a tangent through one of them, we can reduce the curvature evaluation in the end points to the choice of a suitable extrapolation scheme for the angle $\vartheta(s)$ (the ϑ_i are centered in their respective interface segments—see Fig. 4). As it turns out, a linear extrapolation formula [$\vartheta(s(x_1)) = \frac{3}{2}\vartheta_1 - \frac{1}{2}\vartheta_2$] is insufficient for curvature extrapolation. Therefore, we based the curvature calculation in end points on a three-point or quadratic extrapolation scheme, which we then for consistency also used in the evaluation of the angles itself:

$$\vartheta(s(x_1)) = \frac{15}{8}\vartheta_1 - \frac{5}{4}\vartheta_2 + \frac{3}{8}\vartheta_3, \quad (4.3)$$

and analogous formulas for $\vartheta(s(x_e - 0))$, $\vartheta(s(x_e + 0))$, and $\vartheta(s(x_N))$. Four of the nonlinear equations we are going to solve, will then be

$$\vartheta(s(x_1)) = \vartheta(s(x_N)) = 0,$$

$$\vartheta(s(x_e - 0)) = \vartheta_{\alpha}, \quad \vartheta(s(x_e + 0)) = \vartheta_{\beta}. \quad (4.4)$$

The integral equation itself is discretized into boundary elements [20]. This means that the diffusion field as well as its derivative are approximated by functions, not just constant values, on the discretization intervals. Given the discretization points \mathbf{r}_j ($j = 1 \dots N$), we write

$$u_j = u(\mathbf{r}_j), \quad q_j = \left. \frac{\partial u}{\partial n} \right|_{\mathbf{r}_j} \quad (4.5)$$

for their field values. We then interpolate

$$\mathbf{r} = \Phi_1(\xi)\mathbf{r}_j + \Phi_2(\xi)\mathbf{r}_{j+1}, \quad (4.6)$$

$$u(\xi) = \Phi_1(\xi)u_j + \Phi_2(\xi)u_{j+1}, \quad (4.7)$$

$$q(\xi) = \Phi_1(\xi)q_j + \Phi_2(\xi)q_{j+1}, \quad (4.8)$$

where

$$\Phi_1(\xi) = (1 - \xi)/2, \quad \Phi_2(\xi) = (1 + \xi)/2 \quad (4.9)$$

are linear functions, i.e., we take the simplest, namely linear elements. The variable ξ also serves to parametrize the integration interval. Defining

$$\mathbf{s}_j = \mathbf{r}_{j+1} - \mathbf{r}_j = \begin{bmatrix} s_{xj} \\ s_{zj} \end{bmatrix}, \quad s_j = |\mathbf{s}_j| \quad (4.10)$$

(s_j takes on the three values Δs_α , Δs_β , and 0), we have

$$\int_0^{1/2} d\Gamma' \dots = \sum_j \int_{\mathbf{r}_j}^{\mathbf{r}_{j+1}} d\Gamma_j \dots = \sum_j \frac{s_j}{2} \int_{-1}^1 d\xi \dots \quad (4.11)$$

The discretized form of (2.5) then reads

$$\sum_j G_{ij}q_j = \sum_j H_{ij}(u_j - u_\infty), \quad (4.12)$$

where

$$\begin{aligned} G_{ij} = & \sum_m \frac{s_j}{2} \int_{-1}^1 d\xi \Phi_1(\xi) [g(x_i, \xi_i; x_j + \Phi_2(\xi)s_{xj} + m, \xi_j + \Phi_2(\xi)s_{zj}) \\ & + g(x_i, \xi_i; -x_j - \Phi_2(\xi)s_{xj} + m, \xi_j + \Phi_2(\xi)s_{zj})] \\ & + \frac{s_{j-1}}{2} \int_{-1}^1 d\xi \Phi_2(\xi) [g(x_i, \xi_i; x_j - \Phi_1(\xi)s_{x,j-1} + m, \xi_j - \Phi_1(\xi)s_{z,j-1}) \\ & + g(x_i, \xi_i; -x_j + \Phi_1(\xi)s_{x,j-1} + m, \xi_j - \Phi_1(\xi)s_{z,j-1})], \end{aligned} \quad (4.13)$$

$$\begin{aligned} H_{ij} = & \sum_m \frac{s_j}{2} \int_{-1}^1 d\xi \Phi_1(\xi) [h(x_i, \xi_i; x_j + \Phi_2(\xi)s_{xj} + m, \xi_j + \Phi_2(\xi)s_{zj}) \\ & + h(x_i, \xi_i; -x_j - \Phi_2(\xi)s_{xj} + m, \xi_j + \Phi_2(\xi)s_{zj})] \\ & + \frac{s_{j-1}}{2} \int_{-1}^1 d\xi \Phi_2(\xi) [h(x_i, \xi_i; x_j - \Phi_1(\xi)s_{x,j-1} + m, \xi_j - \Phi_1(\xi)s_{z,j-1}) \\ & + h(x_i, \xi_i; -x_j + \Phi_1(\xi)s_{x,j-1} + m, \xi_j - \Phi_1(\xi)s_{z,j-1})]. \end{aligned} \quad (4.14)$$

For $i \neq j$ and $i \neq j \pm 1$, G_{ij} and H_{ij} are evaluated by the four-point Gauss-Legendre integration rule. The other cases need special treatment, because $g(\mathbf{r}, \mathbf{r}')$ diverges logarithmically for $\mathbf{r} \rightarrow \mathbf{r}'$ and $h(\mathbf{r}, \mathbf{r}')$ contains a δ function. The logarithmic divergence is handled by using a Gauss integration rule for integrands exhibiting a logarithmic singularity [21]. Alternatively one could regularize the integral by subtracting out the singular part in analytically integrable form. Our procedure is simpler but can fail, if the 2D distance $|\mathbf{r} - \mathbf{r}'|$ becomes small for points that are far apart along the interface. This situation is very rare in eutectics where the interface does not normally bend back on itself (but see Sec. V). The δ -function singularity plays a role only in the calculation of the diagonal elements of the matrix H . These are therefore not evaluated directly but via the sum rule (see Appendix A), which in matrix notation reads

$$H_{ii} = -1 - \sum_{j \neq i} H_{ij}. \quad (4.15)$$

By this we gain the additional advantage of ensuring global mass conservation.

We are now in a position to set up our system of nonlinear equations for the interface position variables. To this end we impose the integral equation (4.12) every-

where except at the triple point and the end points of the half-cell, which means we take Eqs. (4.12) for $i = 2 \dots N_\beta - 1$ and for $i = N_\beta + 1 \dots N - 1$. The remaining four equations are a consequence of symmetry and the mechanical equilibrium condition. They have already been given above [Eq. (4.4)].

As initial input for the iterative equation solver we normally take two circular segments meeting at the correct pinning angles. Of course, once a solving profile is found, it is used as initial guess to find further solutions at slightly different parameters.

V. NUMERICAL RESULTS

One of the quantities most often referred to in the discussion of lamellar eutectics is the average undercooling, which we can now calculate precisely for any desired parameter combination. It is therefore reasonable to check various statements made about the average undercooling in the literature [8,10]. Figure 5 shows the average undercooling ahead of a pair of lamellae as well as that of each phase separately, in a range of λ values, the smallest of which corresponds to roughly half, and the largest to double, the minimum undercooling value λ_{\min} . In units, where $D = 1$ and $l_T^{\alpha/\beta} = 1$ [22], we have $\lambda_{\min} = 0.0111$ and

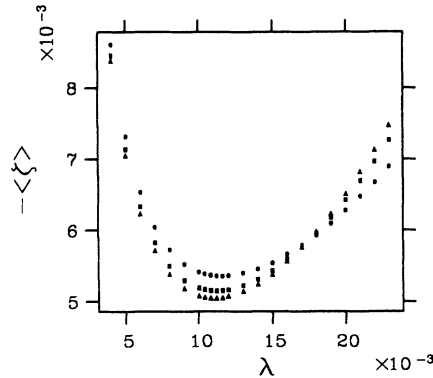


FIG. 5. Negative average interface position, i.e., reduced average undercooling, as a function of the periodicity λ . Squares correspond to a full cell, triangles to the α phase only, circles to the β -phase undercooling. Dynamical parameters: $V=4.0$, $l_T^\alpha=l_T^\beta=1.0$. Material parameters: $d_0^\alpha=d_0^\beta=10^{-5}$, $k_\alpha=0.99$, $k_\beta=1.04$, $u_\infty=0.05$, $\delta=0.3$, $\vartheta_\alpha=0.9$, $\vartheta_\beta=0.7$.

the other relevant length parameters are $l=0.5$ ($V=4.0$) and $d_0^{\alpha/\beta}=10^{-5}$. It is not too surprising that the average undercoolings of the two phases are not equal. The difference, however, is only on the order of 10%. At large λ values, the undercooling of the α phase exceeds that of the β phase because tip splitting becomes important (see also Fig. 8, bottom). The position of the minimum of the curve(s) coincides to within 2% with that calculated from the JH theory. On the other hand, a least-squares fit of a “Jackson-Hunt hyperbola” $\langle \Delta T \rangle = a\lambda + b/\lambda$, shown in Fig. 6, does not describe the data well for $\lambda > \lambda_{\min}$. Moreover, it is not very useful for an accurate determination of the minimum position λ_{\min} , as can be distinguished by the unguided eye.

The purpose of Fig. 7 is to provide verification of an analytic result obtained by Brattkus *et al.* [10], stating that for large thermal gradients the average undercoolings of both phases differ by an amount comparable to their magnitude. The plotted quantities are the same as in Fig. 5; however, in a (relatively) much smaller λ range about the minimum undercooling and for a thermal gra-

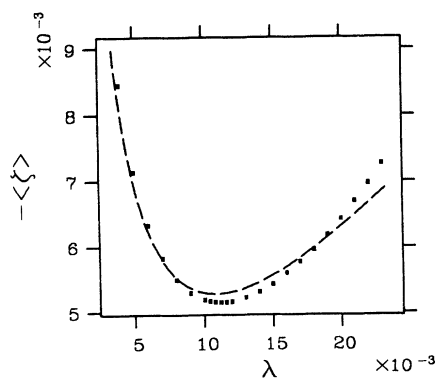


FIG. 6. Average undercooling, as a function of λ , as in Fig. 5. The dashed line is a least-squares fit of a hyperbola $z = a\lambda + b/\lambda$ to the data points.

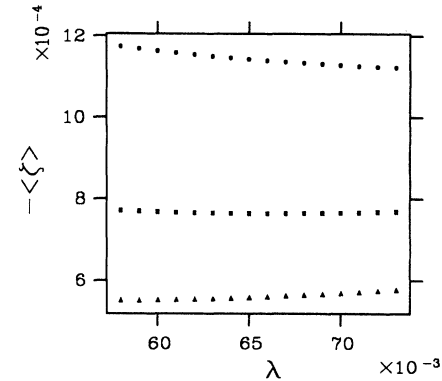


FIG. 7. Average undercooling, as a function of λ , of the entire interface (squares), α lamellae (triangles), and β lamellae (circles), respectively. $l_T^\alpha=l_T^\beta=0.025$, $d_0^\alpha=d_0^\beta=4 \times 10^{-4}$. Other parameters as in Fig. 5.

dient that is larger by a factor of 40 than in the former figure (V is the same). We can indeed confirm the result of Ref. [10]—the β -phase undercooling is roughly twice as large as that of the α phase—and notice that this is probably due to the overall smallness of the average interface distance from zero, which makes any deviation a large deviation. (What is plotted in Figs. 5–7 is $-\langle \xi \rangle = \langle \Delta T \rangle / G$, so the absolute magnitude of the undercooling is actually larger in the last figure than in the two preceding ones.) In addition, we find that for large thermal gradient the position of the minimum undercooling is very different in the two phases. In Fig. 7, we were looking for the minimum of the *total* average undercooling, so the minima of the α and β phase average undercoolings are not even within the domain of λ values plotted.

Let us now turn to a comparison of the interface shapes. In Fig. 8, three solidification structures calculated by solution of the full model (solid lines) are compared with those obtained from the improved JH theory (dashed lines). These structures correspond to the extreme points of Fig. 5: $\lambda=0.005$ and 0.022 —and an intermediate point— $\lambda=0.011$ (which is close to λ_{\min}). Results similar to those to be discussed now have been found for a large variety of λ values. The JH result in general overestimates the magnitude of the undercooling, but its predicted interface profile is remarkably close to the exact one. This is true notwithstanding the statement in Ref. [10] that a JH-type theory can be reliable at large thermal gradients only, i.e., for $l_T/l \ll 1$. In Fig. 8, $l_T/l=2$. Only at the largest wavelength, where tip splitting becomes imminent, does the shape of the JH profile deviate appreciably from the exact one—its excursions about the average interface position are less pronounced, the developing pocket is not as deep as in the true profile.

The reason why the improved JH theory provides accurate results can be traced back to the smallness of the Péclet number. This means that the distortion of the JH diffusion field due to interface excursions about its mean position is of the order of that number. However, as the wavelength λ becomes significantly larger than λ_{\min} the

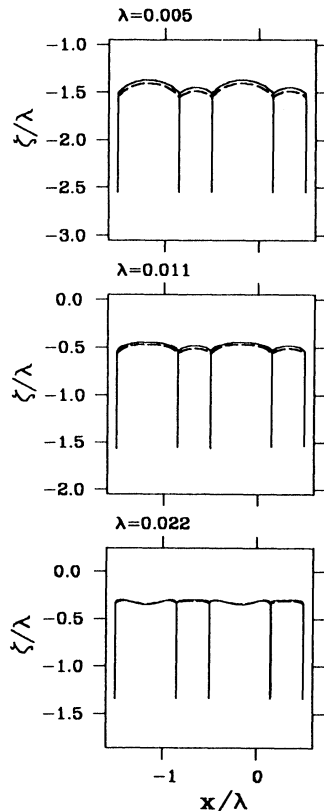


FIG. 8. Interface profiles for the parameters of Fig. 5 and three different λ values. Solid line: exact solution of the model equations; dashed line: improved JH theory.

interface stiffness due to the pinning angle becomes less and less efficient (since the pinning length is of the order of $\sqrt{d_0 l} / \lambda$ in the λ unit). This means that the diffusive effect acts more easily to cause a tip splitting of the interface. As a consequence interface excursions become pronounced and one expects the JH theory to fail above a certain wavelength (see below).

We now leave the JH theory behind in order to proceed to other aspects that have no analog in previous theories of eutectic growth. In Fig. 9, we again present a plot of average undercooling versus periodicity λ . But this time the data points on a vertical line ($\lambda = \text{const}$) do not describe different phases; they show the full-cell undercooling, and all of them correspond to exactly the same system parameters. The only difference is in the creation of these solutions: the iteration was started from different initial guesses. This shows that there is a discrete set of solutions to the nonlinear solidification problem, with different undercoolings and shapes (see Figs. 10 and 11). We have thus demonstrated that even when the wavelength has been selected by the physical system, it still has the choice between different undercoolings for a given velocity. This is akin to the free dendrite which can choose between different discrete velocities for given undercooling—and chooses the largest one. Similarly, one would expect here that the solution with the smallest undercooling is the only stable one. We are now

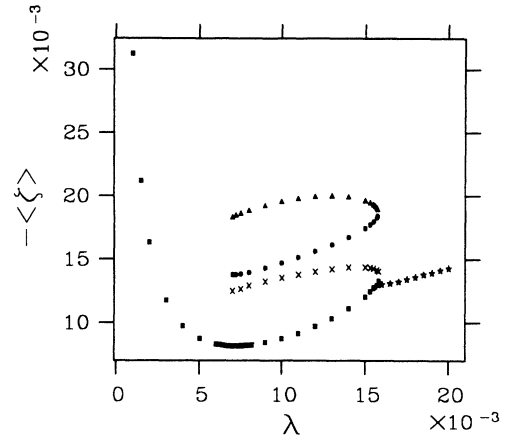


FIG. 9. Average undercooling as a function of λ for four branches of axisymmetric solutions to the model equations (squares, crosses, circles, and triangles) and one branch of tilted solutions. The four branches form two pairs, whose members coalesce into a fold singularity at $\lambda \approx 0.0158$. Beyond this λ value, no axisymmetric solutions could be found. $V = 10.0$, other parameters as in Fig. 5. A similar branch structure was found for $V = 27.5$, $d_0^a = 2 \times 10^{-5}$, $d_0^b = 5 \times 10^{-6}$.

dealing with the full stability problem and hope to report about the results in the future.

The four branches come in two pairs, which join at their large- λ end to form two fold singularities. This type of singularity has also been observed in the bifurcation diagram of directional solidification of dilute alloys [23]. On account of the folds, axisymmetric solutions cease to exist beyond a critical value of λ , which seems to be almost the same for both singularities. On the basis of our present numerical accuracy, we cannot decide whether this apparent equality is exact or only approximate. Figure 9 displays, in addition to the branches mentioned so far, the beginning of a branch of *tilted* solutions, which bifurcates from the lowest axisymmetric branch. We shall not discuss these solutions here; they are only shown to give an indication that the λ value of the folds is not the end of the story—only the end of axisymmetric growth.

The figure conveys the strong impression that there exists an infinity of solution branches, of which we presently see just two repetitive units. The repetition of the bottom structure by the top one is not perfect; they are only similar. Nevertheless, it is an intriguing idea that this repetition of similar structures may continue *ad infinitum*.

It should be added that we have seen four solution branches for other, very different, parameters than that of the figure and that the structure as well as the equality of the critical values λ_c for the two folds seem to be generic features. We are tempted to speculate that this equality is exact. Indeed, the upper branches correspond to “excitedlike” states of the same λ family of the lowest branch. The fold mechanism should then occur at the same λ_c .

Figure 10 shows the four profiles close to the minimum undercooling of the lowest branch, and Fig. 11 gives the

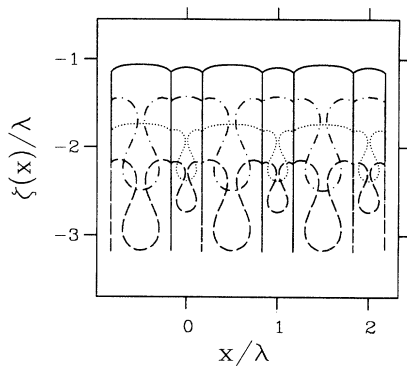


FIG. 10. Interface morphologies for the four solutions of Fig. 9 at $\lambda=0.0075$ (close to λ_{\min} of the lowest branch). The uppermost interface corresponds to the branch depicted by squares in Fig. 9, the lowest to the branch drawn as triangles.

interface structure at a λ value right below that of the folds. The uppermost profile, corresponding to the smallest undercooling, develops, as one would expect, from a convex shape of both phases towards tip splitting of the wider phase when λ is increased (the two capillary lengths are equal here, therefore the wider phase tip splits first). The second profile from the top, which is very similar to the upper one at the large λ value both in shape and position, develops a deep pocket in the α phase when λ is *decreased*. The third profile (dotted line) and the fourth one (dashed line) display tip splitting of the β phase, too, at the large- λ value, where *they* look similar to one another. On decreasing the wavelength, the pockets in the β phase become more pronounced for both profiles, while the third one develops a convex α phase (as in branch 1) and the fourth an ever deepening pocket in the α phase. It is clear that only solution No. 1 corresponds to our (experimentally trained) notion of “proper” behavior as a function of wavelength and hence the others must be the unphysical ones. The main purpose of devoting a few sentences to the upper branches was to demonstrate that the existence of a discrete set of solutions seems to be common to a wide variety of situations (e.g., velocity selection of free dendrites, selection of the

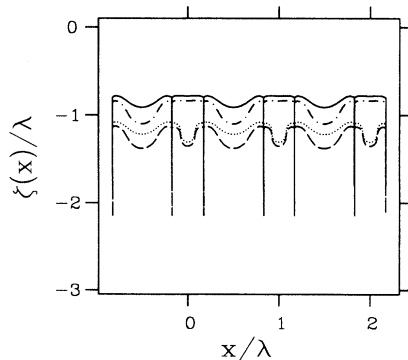


FIG. 11. Same as Fig. 10, but at $\lambda=0.0155$, not far from the folds. The upper and lower pairs of profiles each belong to one fold, and the two interfaces of each pair are close to one another both in appearance and undercooling.

width of Saffman-Taylor fingers, etc.), including eutectic growth—as we know now.

Note that, since the average curvature is fixed by the pinning angles, the difference in average interface position of the solutions forces their volume fractions to be different if global mass conservation is to hold—see Appendix B (although the difference is too small to be well distinguishable in the plot). We have verified that the values of $\langle \xi \rangle_{\alpha/\beta}$ and η for the four solutions indeed satisfy the condition following from global mass conservation, with an accuracy of better than 1%.

We have not included data points of the three top branches in Fig. 9 for $\lambda < 0.007$, although we calculated some. The reason is that below this value the pockets in these solutions have closed so far that the interaction between the approaching parts of the indented phase(s) is no longer handled accurately by our code (see Sec. IV). The results that we have suggest that the upper branches also run through a minimum, whose abscissa is not too far from λ_{\min} of the lowest branch. In fact, for any solution that exists down to arbitrarily small λ values, the undercooling must rise again, because it will be dominated eventually by the curvature term, whose contribution to the average undercooling is exactly the same for all solutions at a given λ . [This is so, because the η dependence in Eqs. (3.11) and (3.12) cancels for the average over a full cell.] It seems very likely that at least branch No. 2 (depicted by crosses) does exist for small λ , because unlike branches No. 3 and No. 4 it does not have a partner with which it could annihilate in a second fold. Whether this will actually happen in the cases of branches No. 3 and No. 4, is an open question, which we tend to answer in the negative.

VI. SIMILARITY EQUATION

This section is devoted to a complete derivation of a generalization of the nonlinear similarity equation of which we have already given a brief account in Ref. [12]. The similarity equation is valid for small Péclet numbers, which is the experimentally relevant case. We will discuss some of its far-reaching consequences.

As we saw before, the eutectic system is governed by four relevant length parameters, namely the diffusion length l , the capillary length d_0 , the thermal length l_T , and the periodicity λ of the pattern. Actually there are six lengths, because we have *two* capillary lengths d_0^α and d_0^β as well as two thermal lengths l_T^α and l_T^β . However, on taking ratios again to reduce the number of variables by 1, we notice that *for a given material* two of these ratios, namely d_0^α/d_0^β and l_T^α/l_T^β , are constant. They will not be as easily varied in a particular series of experiments as the other, *dynamical* quantities, for which we choose now $P = \lambda/l$, $\sigma = ld_0^\alpha/\lambda^2$, and $\chi = l/l_T^\alpha$.

For the discovery of any *geometric* similarity property of the pattern it is obviously necessary to rewrite the equations of motion in units of λ . Let us do so first with the Gibbs-Thomson equation. Equation (2.2) transforms into

$$u = \begin{cases} -\lambda\xi/l_T^\alpha - d_0^\alpha\kappa/\lambda, & \alpha \text{ phase} \\ \lambda\xi/l_T^\beta + d_0^\beta\kappa/\lambda, & \beta \text{ phase} . \end{cases} \quad (6.1)$$

Notice that it is possible to factor out the Péclet number,

$$u = -P\epsilon(x)(\chi\zeta + \psi\sigma\kappa) \equiv P\bar{u}(x), \quad (6.2)$$

where ϵ and ψ are piecewise-constant functions, defined by

$$\epsilon(x) = \begin{cases} 1, & \alpha \text{ phase} \\ -l_T^\alpha/l_T^\beta, & \beta \text{ phase} \end{cases} \quad (6.3)$$

and

$$\psi(x) = \begin{cases} 1, & \alpha \text{ phase} \\ l_T^\beta d_0^\beta / l_T^\alpha d_0^\alpha, & \beta \text{ phase} . \end{cases} \quad (6.4)$$

For definiteness, we choose the origin of the x axis to align with a triple point to the left of an α -phase lamella, i.e., we have an α phase in the interval $(0, \eta)$ and a β phase for $x \in (\eta, 1)$. In our calculation presented earlier [12], $\psi(x)$ was equal to 1 identically, and $\epsilon(x)$ switched

between +1 and -1.

Using Eq. (2.4), we obtain a similar expression for the normal derivative

$$\frac{1}{Pn_z} \frac{\partial u}{\partial n} = 2\{P\epsilon(x)[1-k(x)](\chi\zeta + \psi\sigma\kappa) - H(x)\}, \quad (6.5)$$

where we have suppressed the x dependence of ψ , ζ , and κ in the parentheses and have defined

$$k(x) = \begin{cases} k_\alpha, & \alpha \text{ phase} \\ k_\beta, & \beta \text{ phase} , \end{cases} \quad (6.6)$$

$$H(x) = \begin{cases} \delta, & \alpha \text{ phase} \\ \delta - 1, & \beta \text{ phase} . \end{cases} \quad (6.7)$$

Inserting (6.2) and (6.5) into the integral equation (2.8), we arrive at

$$\begin{aligned} \frac{-\epsilon(x)}{2} [\chi\zeta(x) + \psi(x)\sigma\kappa(x)] &= \frac{u_\infty}{P} - \frac{1}{2\pi} \int_{-\infty}^{\infty} dx' e^{-P\Delta\xi} K_0(P\rho) \{P\epsilon(x') [1-2k(x')] (\chi\zeta + \psi\sigma\kappa) - 2H(x')\} \\ &\quad - \frac{1}{2\pi} \int_{-\infty}^{\infty} dx' e^{-P\Delta\xi} K_1(P\rho) \frac{\Delta\xi - \Delta x \xi_{x'}}{\rho} P\epsilon(x') (\chi\zeta + \psi\sigma\kappa) . \end{aligned} \quad (6.8)$$

We wish to investigate, with due care, how Eq. (6.8) behaves in the limit $P \rightarrow 0$, corresponding to the experimentally relevant situation of small Péclet number ($P \lesssim 0.01$).

Let us call the first integral in (6.8) I_1 , the second, which we will consider first, I_2 . On naively taking the limit $P \rightarrow 0$ in the integrand of I_2 , we obtain, using the small argument expansion $K_1(P\rho) \simeq 1/P\rho$,

$$\begin{aligned} -\frac{1}{2\pi} \int_{-\infty}^{\infty} dx' \frac{\Delta\xi - \Delta x \xi_{x'}}{\rho^2} \\ \times \epsilon(x') [\chi\zeta(x') + \psi(x')\sigma\kappa(x')] \equiv I_{20} . \end{aligned} \quad (6.9)$$

Of course, it is not obvious *a priori* that we are allowed to do this, because the integration extends to infinity and hence $P\rho$ inside the integral becomes infinitely large no matter how small P , as long as P is nonzero. Even worse, at first sight it looks as if the integral I_{20} is *divergent*. The most slowly decaying term of the integral contains the factor $\Delta x \xi_{x'}/\rho^2$, which for large x' goes as $1/|x'-x|$, a quantity whose integral diverges logarithmically. Note that the term $\Delta\xi/\rho^2$ is perfectly integrable, since $\Delta\xi$ is a bounded function. Also the limit $\rho \rightarrow 0$ poses no problem, because

$$\frac{\Delta\xi - \Delta x \xi_{x'}}{\rho^2} \xrightarrow{\Delta x \rightarrow 0} \frac{\xi_{x'x'}}{2(1+\xi_{x'}^2)} . \quad (6.10)$$

So we are left with the first discussed term, which might render the integral divergent and actually does so

for arbitrary periodic functions $\zeta(x)$ [24]. However, it can be shown that the integral is convergent, if $\zeta(x)$ is *axi-symmetric*. The proof is given in Appendix C for mathematically interested readers; suffice it here to say that the convergence is of the same type as that of the integral of $\sin(x)/x$.

Once we are sure that I_{20} is convergent, what remains to be shown is that it is actually the limit for $P \rightarrow 0$ of I_2 , i.e., that the latter integral converges uniformly as P is sent to zero. Again, we relegate the proof to the Appendix.

In order to treat I_1 , we first introduce the abbreviations

$$G(x') = -\epsilon(x') [1-2k(x')] (\chi\zeta + \psi\sigma\kappa) , \quad (6.11)$$

$$L_P(x') = (e^{-P\Delta\xi} - 1) [PG(x') + 2H(x')] . \quad (6.12)$$

In order to perform the limit $P \rightarrow 0$ for I_1 , we split the integral into three terms as follows:

$$\begin{aligned} I_1 &= \frac{1}{2\pi} \int_{-\infty}^{\infty} dx' e^{-P\Delta\xi} [K_0(P\rho) - K_0(P|\Delta x|)] \\ &\quad \times [PG(x') + 2H(x')] \\ &\quad + \frac{1}{2\pi} \int_{-\infty}^{\infty} dx' K_0(P|\Delta x|) L_P(x') \\ &\quad + \frac{1}{2\pi} \int_{-\infty}^{\infty} dx' K_0(P|\Delta x|) [PG(x') + 2H(x')] \end{aligned} \quad (6.13)$$

and call the three integrals I_{1a} , I_{1b} , and I_{1c} , respectively. The proof that I_{1a} converges uniformly as a function of P

is then analogous to the one given for I_2 in Appendix C. We are therefore allowed to replace K_0 by its small argument expansion $K_0(P\rho) \simeq -\ln P\rho$ in I_{1a} and obtain

$$\lim_{P \rightarrow 0} I_{1a} = \frac{1}{\pi} \int_{-\infty}^{\infty} dx' \ln \frac{|\Delta x|}{\rho} H(x'). \tag{6.14}$$

The two remaining integrals can be considered together. All three functions $G(x')$, $H(x')$, and $L_P(x')$ are periodic with period 1 and can be expanded in Fourier series. We write the series in the form we need inside the integral:

$$G(x') = \sum_{n=-\infty}^{\infty} b_n e^{-i2\pi n \Delta x}, \tag{6.15}$$

$$H(x') = \sum_{n=-\infty}^{\infty} c_n e^{-i2\pi n \Delta x}, \tag{6.16}$$

$$L_P(x') = \sum_{n=-\infty}^{\infty} d_n(P) e^{-i2\pi n \Delta x}, \tag{6.17}$$

where all the Fourier coefficients depend parametrically on x , but only the coefficients of $L_P(x')$ are P dependent. Furthermore, we know that the $d_n(P)$ go to zero, when P is taken to zero. Since the three functions are piecewise smooth, their Fourier series can be integrated term by term and this property still holds for the series multiplied by K_0 . Changing the integration variable to $y = x - x'$, we have for I_{1c}

$$\begin{aligned} I_{1c} &= \frac{1}{2\pi} \int_{-\infty}^{\infty} dy K_0(P|y|) \left[P \sum_{n=-\infty}^{\infty} b_n e^{-i2\pi ny} \right. \\ &\quad \left. + 2 \sum_{n=-\infty}^{\infty} c_n e^{-i2\pi ny} \right] \\ &= \frac{1}{2} \sum_{n=-\infty}^{\infty} \left[\frac{P b_n}{[P^2 + (2\pi n)^2]^{1/2}} + \frac{2c_n}{[P^2 + (2\pi n)^2]^{1/2}} \right], \end{aligned} \tag{6.18}$$

where we have used (Ref. [25], No. 6.671,14)

$$\int_0^{\infty} dx K_0(\beta x) \cos(\alpha x) = \frac{\pi}{2(\alpha^2 + \beta^2)^{1/2}} \tag{6.19}$$

In a similar manner, we obtain

$$I_{1b} = \sum_{n=-\infty}^{\infty} \frac{d_n(P)}{2[P^2 + (2\pi n)^2]^{1/2}}. \tag{6.20}$$

We can now take the limit $P \rightarrow 0$, which yields

$$\lim_{P \rightarrow 0} I_{1b} = \lim_{P \rightarrow 0} \frac{d_0(P)}{2P}, \tag{6.21}$$

$$\lim_{P \rightarrow 0} \left[I_{1c} - \frac{c_0}{P} \right] = \frac{1}{2} b_0 + \sum_{\substack{n=-\infty \\ n \neq 0}}^{\infty} \frac{c_n}{2\pi |n|}. \tag{6.22}$$

Finally, we have to evaluate the Fourier coefficients b_0 , c_n , and $d_0(P)$ and to discuss the divergent terms $\propto 1/P$. In the first task, the simplest case is the coefficients c_n , because $H(x)$ is a piecewise constant function. We have

$$c_0 = \langle H(x) \rangle = \delta + \eta - 1, \tag{6.23}$$

$$c_n = e^{i2\pi n(x - \eta/2)} \frac{\sin(n\pi\eta)}{n\pi}. \tag{6.24}$$

The two other coefficients are obtained in the form of integrals:

$$\begin{aligned} b_0 &= \langle G(x) \rangle \\ &= -(1 - 2k_\alpha) \int_0^\eta dx' [\chi \zeta(x') + \sigma \kappa(x')] \\ &\quad + (1 - 2k_\beta) \int_\eta^1 dx' \left[\frac{l_T^\alpha}{l_T^\beta} \chi \zeta(x') + \frac{d_0^\alpha}{d_0^\beta} \sigma \kappa(x') \right], \end{aligned} \tag{6.25}$$

and

$$\begin{aligned} d_0(P) &= \langle L_P(x) \rangle \\ &= \int_0^1 dx' (e^{-P\Delta \xi} - 1) [PG(x') + 2H(x')], \end{aligned} \tag{6.26}$$

which leads to

$$\lim_{P \rightarrow 0} \frac{d_0(P)}{2P} = - \int_0^1 dx' \Delta \xi H(x'). \tag{6.27}$$

On collecting the terms for our final equation we find [in Eqs. (6.8) and (6.22)] two quantities which diverge as $1/P$. Their sum is $(u_\infty + \delta + \eta - 1)/P$ and it is finite. We show in Appendix B that as a result of mass conservation on the global scale we have

$$\begin{aligned} \frac{u_\infty + \delta + \eta - 1}{P} &= -k_\alpha \int_0^\eta dx' [\chi \zeta(x') + \sigma \kappa(x')] \\ &\quad + k_\beta \int_\eta^1 dx' \left[\frac{l_T^\alpha}{l_T^\beta} \chi \zeta(x') + \frac{d_0^\alpha}{d_0^\beta} \sigma \kappa(x') \right], \end{aligned} \tag{6.28}$$

i.e., this term and the k_α and k_β terms stemming from $b_0/2$ cancel each other [26]. Therefore, the similarity equation reads

$$\begin{aligned} \frac{-\epsilon(x)}{2} [\chi \zeta(x) + \psi(x) \sigma \kappa(x)] &= -\frac{1}{2} \int_0^1 dx' \epsilon(x') [\chi \zeta(x') + \psi(x') \sigma \kappa(x')] - \int_0^1 dx' \Delta \xi H(x') \\ &\quad + \sum_{n=1}^{\infty} \frac{\sin(n\pi\eta)}{(n\pi)^2} \cos \left[2n\pi \left[x - \frac{\eta}{2} \right] \right] + \frac{1}{\pi} \int_{-\infty}^{\infty} dx' \ln \frac{|\Delta x|}{\rho} H(x') \\ &\quad - \frac{1}{2\pi} \int_{-\infty}^{\infty} dx' \frac{\Delta \xi - \Delta x \zeta_{x'}}{\rho^2} \epsilon(x') [\chi \zeta(x') + \psi(x') \sigma \kappa(x')]. \end{aligned} \tag{6.29}$$

Let us first stress that this result is nontrivial. While one could expect that taking the limit $P \rightarrow 0$ is feasible and that the final result would not contain P anymore (unless all terms became zero), it could have reduced to a trivial identity. This is not the case.

An instructive special case of Eq. (6.29) is the planar interface. Inserting $\Delta\zeta=0$ into the similarity equation, the second, fourth, and fifth terms on the right-hand side vanish, and we recover the JH formula (3.5) for $z=\bar{\zeta}$. Equation (6.29) may constitute a basis for higher-order expansions beyond the JH approximation. This is, however, not attempted here.

The equation states that at small nonzero Péclet numbers, where it may be used, for continuity reasons, as an approximation to the full equation (6.8), the properties of the solidification pattern depend on the two dynamical parameters χ and σ only and not on P itself. In other words, the Péclet number has scaled out of the original equation. (Note that in applying the equation for nonzero P , we reintroduce a weak P dependence via the quantity η , which depends on P through global mass conservation. Of course it is legitimate to avoid this by replacing η with its zeroth-order term in an expansion in powers of P , which is $1-u_\infty-\delta$.)

We gather from the similarity equation that if we change any set of fundamental parameters l , l_T , d_0 , and λ , such that their combinations χ and σ remain unaltered, the pattern *as measured in units of λ* remains unchanged. In physical units, the pattern may shrink or expand, according to the change in λ , but it remains *similar* to the original.

An example for a change that keeps χ and σ constant, would be a multiplication of λ by a (positive) factor α and of l as well as l_T by α^2 (at fixed d_0). In terms of experimental quantities this means that V and G both have to be multiplied by α^{-2} .

Another possibility, which is of interest for numerical investigations, is to divide l and l_T by α (> 1) and multiply d_0 by α . Since the computational expenditure increases with the effective interface size, which in turn scales with l , while changes of d_0 and l_T enter the local dynamics only, it is clear that much CPU time can be saved by looking at a system obtained by an appropriate similarity transformation. In going from the original system to the one scaled by α one changes the Péclet number. This sets an upper limit to this type of manipulation—the Péclet number must be kept much smaller than 1. Nevertheless, we have compared some runs at $V=0.1$, $d_0=10^{-5}$ with others at $V=4.0$, $d_0=4 \times 10^{-4}$ and a 40 times larger thermal gradient, and we find that in the second case the CPU time is decreased by a factor of roughly 40, while the minimum undercooling wavelength is reproduced within approximately 1% accuracy. (The method is useful as long as the desired error bounds for the results are not smaller than the effects of the residual P dependence, which must be present in any exact solution, owing to global mass conservation.)

Let us discuss and numerically check some consequences of the similarity equation. First of all, it is possible to check it directly. We have calculated the solidification profile for a sequence of velocities V and

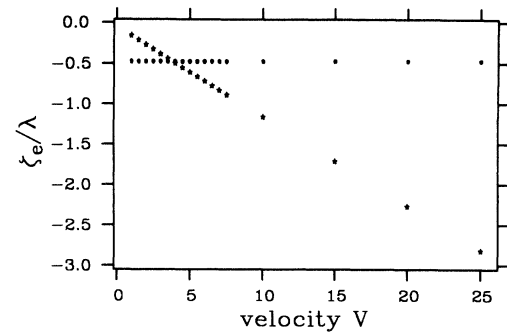


FIG. 12. Vertical position of the eutectic point as a function of velocity. The material parameters are the same as in Fig. 5. The data represented by stars correspond to $l_T^\alpha=l_T^\beta=1.0$. V and λ were varied simultaneously such that $\lambda^2 V = \text{const}$ (and hence $\sigma = \text{const}$, because $d_0^{g/\beta}$ were kept fixed). In this way, λ was varied between 4.7×10^{-3} and 2.3×10^{-2} . $\sigma=0.037$. To obtain the data drawn as circles, V and λ were chosen as before, but $l_T=l_T^\alpha=l_T^\beta$ was varied as well to keep l/l_T constant. The point of intersection of both curves corresponds to $l_T=1.0$; for smaller V , l_T is larger (extending up to $l_T=3.8$), for larger V , l_T decreases (down to $l_T=0.15$). $\chi=0.53$. The λ range of the figure corresponds to a change in the Péclet number from $P=0.012$ at the smallest velocity to $P=0.059$ at the largest V .

changed λ such that σ , commonly believed to be the most relevant parameter, was constant. All the other parameters, in particular l_T , were not changed. In a second sequence of calculations, we took the same V and λ values as before but changed l_T accordingly to keep χ constant, too. In Fig. 12 we plot the z coordinate of the triple point for some of these runs. The stars represent the case $(\sigma, l_T) = \text{const}$; the circles the case $(\sigma, \chi) = \text{const}$, in a velocity range from 1 to 25. It is clearly seen that only in the second case does ζ_e remain constant in reduced units. A plot of $\langle \zeta \rangle$ looks completely the same; we have not included it here since on the scale of the figure the points for ζ_e and $\langle \zeta \rangle$ would touch each other. Probably even more impressive is a comparison of the profiles themselves. In Fig. 13 we have, on the left-hand side 25 profiles from runs with constant σ and l_T at different velocities. Believe it or not, on the right-hand side there are also 25 profiles, now with χ kept constant instead of l_T . We have reduced the line thickness in this figure in order to make any differences between the similar profiles more conspicuous—an unsuccessful attempt. The position of the profiles in the right-hand-side panel corresponds to the point of intersection of the two “curves” of Fig. 12.

Note that χ is proportional to G/V , a parameter that is at the disposal of experimentalists. Therefore, the drastic difference predicted between the two situations of Fig. 13 is not devoid of experimental testability.

Our second observation is that, no matter how the wavelength selection mechanism operates, it must provide an additional relation between χ and σ , which implies a scaling law of the form

$$\lambda \simeq \sqrt{d_0 l} f(l/l_T), \quad (6.30)$$

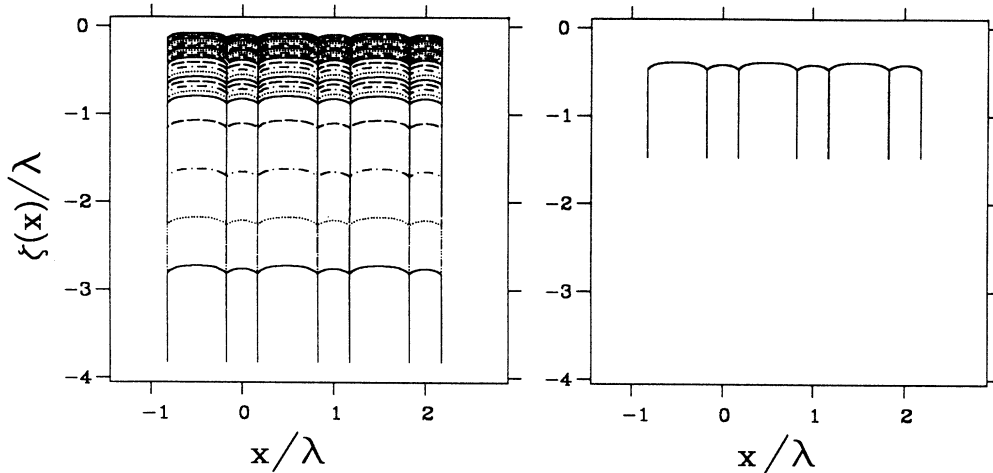


FIG. 13. Left: the profiles corresponding to the stars in Fig. 12 (plus some whose data points were left out in Fig. 12 to avoid crowding). Right: the profiles corresponding to the circles in Fig. 12.

or, less transparent but in the correct parameters,

$$\sqrt{1/\sigma} \approx f(\chi). \quad (6.31)$$

Up to now, it has been the conventional wisdom that the selected wavelength in eutectic growth scales as $\lambda \approx V^{-1/2}$, notwithstanding the fact that there are quite a few experiments that show deviations from this law at low velocities with exponents down to 0.3 instead of $\frac{1}{2}$ [13]. An explanation of the conventional scaling law seemed to be provided by the hypothesis that the operating point of the eutectic is determined by the minimum undercooling, since λ_{\min} was assumed to scale as $V^{-1/2}$ according to the JH theory. Combined with our similarity equation, the statement would then be that $f(\chi)$ is constant.

This prediction can be checked by numerical calculation of $f(\chi)$ for the minimum undercooling point. We calculated enough profiles so that splining their average undercoolings given as a function of λ and determining the minimum of the spline interpolant provided a sufficiently accurate value for λ_{\min} . This procedure was repeated for several velocities to obtain points of the curve $f(l/l_T)$, which we conveniently present as a function of V (l_T was kept constant).

Figure 14 shows the result. The logarithm of $\lambda V^{1/2}$ is

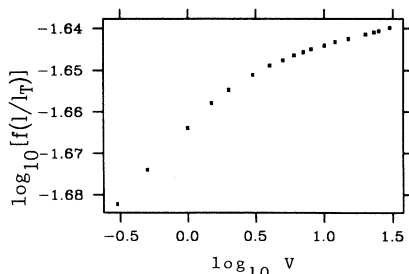


FIG. 14. Scaling function $f(l/l_T) = \lambda V^{1/2}$ as a function of the velocity in double-logarithmic representation. Here, λ is the wavelength corresponding to the minimum undercooling point, which is determined numerically as described in the text.

plotted against the logarithm of V . Any straight line with slope a means a power law $\lambda \propto V^{a-1/2}$, i.e., a describes the deviation of the scaling exponent from $-\frac{1}{2}$. We can distinguish two regions with roughly constant slope in the figure. In the low-velocity one, $a \approx 0.033$, while at higher velocities, $a \approx 0.008$. The tendency clearly agrees with the experimental results described in Ref. [13], even though our low-velocity exponent -0.466 is still very close to $-\frac{1}{2}$. However, there are several parameters whose change may influence the value of the exponent and which we have not yet found time to vary over a large range. For example, an alteration of the ratios l_T^α/l_T^β or d_0^α/d_0^β changes the functions $\epsilon(x)$ and/or $\psi(x)$.

We have verified for different parameter sets that the qualitative behavior of the scaling function is the same, i.e., $f(\chi)$ bends downward at small velocities, again with very small deviations of the exponent from $-\frac{1}{2}$. However, we have not pursued this any further (in an attempt to find parameters that produce a larger deviation), mostly for cost reasons.

In any case, it can be stated that a high enough velocities the parameter χ becomes irrelevant and the scaling is determined by σ alone. Expressed differently, $f(l/l_T)$ becomes a constant for $l \rightarrow 0$, i.e., $f(\chi)$ is continuous and nonzero at $\chi=0$.

Finally, we can check in a similar way the predictions of JH concerning the scaling of the undercooling ΔT as a function of velocity. In Fig. 15 we present $\Delta T/V^{1/2}$ as a function of V in a double-logarithmic plot. A straight line would correspond to a law of the type $\Delta T \propto V^{b+1/2}$. However, there is not really a straight line. At high velocities the scaling seems to saturate to an exponent $\frac{1}{2}$, but at low velocities the curve is never straight, so there is no constant exponent. Nevertheless, the deviation from the expected scaling $\Delta T \propto V^{1/2}$ is very small here, too. If we “force” a straight line through the three points at the lowest velocities, we obtain $b=0.014$.

It should be recalled here that there is up to now no proof that the selected wavelength corresponds exactly to

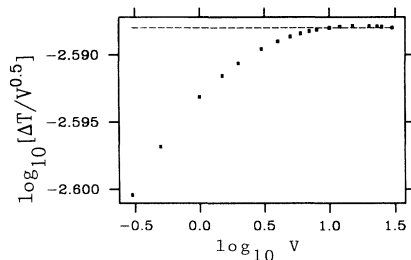


FIG. 15. Scaling behavior of ΔT as a function of the velocity for the minimum undercooling point.

the minimum undercooling point. It would then be possible that the larger deviation, in experiments, of the discussed exponents from $-\frac{1}{2}$ and $\frac{1}{2}$ is explicable by the fact that the operating point is not the one which provides the minimum undercooling.

Yet we can make another, much stronger, statement about a power-law dependence of wavelength selection, which immediately suggests a new experiment for its verification. Relation (6.30) tells us that if we keep l/l_T (i.e., G/V) constant, we will have $\lambda \propto V^{-1/2}$ exactly. This is absolutely independent of how the selection mechanism operates, because it is a consequence only of the facts that wavelength selection must provide *some* relation of the type (6.30) and that the function f remains constant, if its argument is constant. The range of validity of this new scaling relation is only limited by the requirement that the Péclet number must be small. To verify it experimentally, we propose to take one of the compounds of Ref. [13], for which at low velocities strong deviations of the exponent from $-\frac{1}{2}$ have been seen (at constant thermal gradient) and repeat the experiment, measuring the wavelength as a function of velocity *while keeping the ratio of velocity and thermal gradient constant*. This should result in a scaling law $\lambda^2 V = \text{const}$ down to the smallest velocities.

VII. CONCLUDING REMARKS

We have studied lamellar eutectic growth by numerical solution of the basic model equations for a reasonably large set of different parameter combinations. Comparing our calculated front shapes and quantitative data with previous analytic theories, such as the JH theory [8] and the work of Brattkus *et al.* [10], we can ascertain that the critique of the former by the latter is justified. Namely, the JH theory should be expected to work only for large thermal gradients on account of the planar interface approximation, but for large thermal gradients the equal undercooling assumption is a poor approximation. On the other hand, an improved JH theory, not employing that assumption, does remarkably well as far as front shapes and average positions are concerned, even for medium thermal gradients, when the interface is not close to planar. The accuracy of the improved JH theory becomes poorer as tip splitting sets in, and the JH theory does not “see” the fold—it produces “solutions” with strong tip splitting well beyond λ_c . Also we have not

found any indication that there might be a discrete degeneracy of solutions to the pertinent second-order (non-linear) differential equations.

The discovery of a discrete set of solutions (belonging to the same symmetry group) in the eutectic system is one new aspect of our calculations. It has led to the identification of a distinguished wavelength λ_c in addition to the minimum undercooling point (and the point of bifurcation to tilted solutions). It will be a task of future theoretical developments to clarify the role of this point and its possible relations to wavelength selection (if any). We have not yet found more than four axisymmetric branches for any system, and while Fig. 9 suggests, as has been discussed, the existence of additional solutions, it is hard to guess, after inspection of Figs. 10 and 11, what these solutions might look like. If one reduces d_0^β sufficiently, the morphologies of branches No. 2 and No. 3 interchange, i.e., the solution coalescing into a fold with branch No. 1 has a pocket in the β phase instead of the α one. Interesting things may happen when the competition between the larger width of phase α and the smaller capillary length of phase β is such that the system cannot decide what the morphology of the second branch should be (the problem can be seen most clearly in a system with $\eta = \frac{1}{2}$, a symmetric phase diagram, and equal capillary lengths). To our knowledge, morphologies corresponding to higher branches in Fig. 11 can, at best, be met as transients in experiments. A velocity jump by about a factor of 4 is likely to “push” the interface wavelength towards the fold singularity (since $\lambda_c/\lambda \approx 2$ and $\lambda^2 V \approx \text{const}$) rather than to excite the interface into higher branches. Indeed, the response time of the mean front position (or undercooling) due to a velocity jump seems to be small in standard experiments in comparison to the time scale for wavelength adjustment. One therefore expects, in general, the whole structure to undergo a parity-breaking transition as a result of a velocity jump.

Our second main result is the analytic reduction of the full boundary integral equation to a similarity equation that depends on one parameter less. In the limit of *vanishing* Péclet number the similarity equation is identical with the boundary integral equation. For *small* Péclet numbers, it constitutes a useful approximation. We have demonstrated some of its direct consequences numerically. Among these were the geometric similarity of solutions corresponding to different parameter sets, if only the parameter combinations χ and σ were kept constant, and the constancy of the scaled average undercooling as well as the position of the triple point, under the same circumstances.

Furthermore, we have extracted scaling relations from the similarity equations which allow to explore numerically, how the selected wavelength should scale in the ordinary experimental situation (constant thermal gradient), if it is determined by the minimum undercooling. We found agreement with the experimental observation [13] that the scaling is of the form $\lambda \approx V^{-\beta}$, with β smaller than $\frac{1}{2}$ at low velocities and approaching $\frac{1}{2}$ at high velocities. From the general form of the scaling law, we moreover predict that in a different experiment, where the ratio of velocity and thermal gradient is kept fixed,

the analogous scaling exponent should be exactly $\frac{1}{2}$. We hope our prediction will be put to the test soon, by an experiment of the suggested type.

We close with an outlook on important work that remains to be done: the linear stability analysis of the symmetric states.

First we will consider the soft-phase instability. As the full equations are invariant under a constant phase shift, the Goldstone mode is a neutral mode of the linearized dynamical equations. It is therefore natural to expect long-wavelength phase fluctuations to be dangerous. Using the spirit of the method employed in directional solidification of dilute alloys [27] it is possible to extract from the full equations the part that is relevant to the phase dynamics. This extraction requires some analytical sophistication, but offers the advantage of avoiding an effort to locate the instability close to the center of the first Brillouin-like zone by a forward stability analysis.

The second aspect of our outlook is related to the search for oscillatory modes, for which there is experimental evidence. A full linear stability analysis will then be necessary, without resorting to the (advantageous) quasistationary approximation, since this would not be legitimate for Hopf-type instabilities. This analysis would permit us to specify precisely the appearance of different kinds of instabilities. The ‘‘optical-like’’ modes, commonly observed in various experiments, take place with a spatial period that is about twice as large as the basic one (for the steady state). Moreover, our analysis of parity-breaking transitions, on which we will give a separate discussion, tells us that parity-broken states result as a quasi-period-doubling bifurcation. We are tempted to conjecture that an interplay between parity-broken states and ‘‘optical’’ modes constitutes a prelude to a chaotic regime.

APPENDIX A: THE SUM RULE

Our derivation of the sum rule starts from the observation that $u \equiv u_0$ with an arbitrary constant u_0 solves the diffusion equation (2.1). This means that the integral equation (2.5) is fulfilled with u replaced by u_0 and Γ_{sl} replaced by any *closed* contour. [In (2.5) the contour was also closed originally but the closing pieces were at infinity and could be dropped because $u = u_\infty$ and $\partial u / \partial n' = 0$ there [18].] In the present context the most useful closure of the integration contour is obtained by adding to Γ_{sl} a piece Γ_Z running from $x' = \infty$ to $x' = -\infty$ at a value $z' = Z > 0$ and joining it to Γ_{sl} at the infinitely far end points by pieces $\Gamma_{\parallel 1}$ and $\Gamma_{\parallel 2}$, which are parallel to the z axis (see Fig. 16). We call the total contour Γ , and after division by $u_0 - u_\infty$ (taken $\neq 0$) the integral equation becomes

$$\int_{\Gamma} d\Gamma' h(\mathbf{r}, \mathbf{r}') = 0. \quad (\text{A1})$$

Written out explicitly in terms of the modified Bessel functions, Eq. (2.6) reads

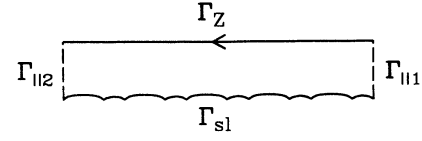


FIG. 16. Integral contour used in the derivation of the sum rule.

$$h(\mathbf{r}, \mathbf{r}') = \frac{1}{2\pi l} \exp\left[\frac{-(z-z')}{l}\right] \times \left[-n'_z K_0\left[\frac{|\mathbf{r}-\mathbf{r}'|}{l}\right] - \frac{\mathbf{n}'(\mathbf{r}'-\mathbf{r})}{|\mathbf{r}-\mathbf{r}'|} \times K_1\left[\frac{|\mathbf{r}-\mathbf{r}'|}{l}\right] \right] - \frac{1}{2} \delta(\mathbf{r}-\mathbf{r}'). \quad (\text{A2})$$

Let us require that $\mathbf{r} [= (x, z)]$ does not lie on Γ_Z , i.e., $z \neq Z$, so the δ -function term can be omitted in the integral on contour Γ_Z , whose contribution to the full integral (A1) is then

$$\int_{\Gamma_Z} d\Gamma' h(\mathbf{r}, \mathbf{r}') = \int_{-\infty}^{\infty} dx' h(\mathbf{r}, \mathbf{r}') = \frac{1}{2\pi l} e^{\Delta z/l} \int_{-\infty}^{\infty} dy \left[K_0((y^2 + \Delta z^2)^{1/2}/l) + \frac{\Delta z}{(y^2 + \Delta z^2)^{1/2}} \times K_1((y^2 + \Delta z^2)^{1/2}/l) \right]. \quad (\text{A3})$$

In the first of these two equalities, we have used that $d\Gamma' = -dx'$ on Γ_Z and interchanged the integration boundaries. In the second we have exploited that \mathbf{n}' is equal to the negative unit vector in z direction ($\Rightarrow n'_z = -1$), introduced the abbreviations $\Delta z = z' - z = Z - z$, and changed the variable of integration to $y = x' - x$.

We call the first integral on the right-hand side of the last equality I_a , the second I_b . Both integrals can be evaluated exactly with the help of (Ref. [25], No. 6.593,3)

$$\int_0^{\infty} dx K_\nu(\alpha \sqrt{x^2 + z^2}) \frac{x^{2\mu+1}}{(x^2 + z^2)^{\nu/2}} = \frac{2^\mu \Gamma(\mu+1)}{\alpha^{\mu+1} |z|^{\nu-\mu-1}} K_{\nu-\mu-1}(\alpha|z|), \quad (\text{A4})$$

which we have written for real z and which holds for $\alpha > 0$, $\Re(\mu) > -1$. Choosing $\mu = -\frac{1}{2}$, we immediately obtain

$$I_a = \sqrt{2\pi l |\Delta z|} K_{-1/2}(|\Delta z|/l), \quad (\text{A5})$$

$$I_b = \text{sgn}(\Delta z) \sqrt{2\pi l |\Delta z|} K_{1/2}(|\Delta z|/l). \quad (\text{A6})$$

But the half-integer-order Bessel functions are expressible

via elementary functions, and we have (see Ref. [26], No. 8.469,3)

$$K_{\pm 1/2}(z) = \sqrt{\pi/2z} e^{-z}. \quad (\text{A7})$$

Therefore, we obtain

$$I_a = \pm I_b = \pi l e^{-|\Delta z|/l}, \quad (\text{A8})$$

where the sign of I_b is equal to the sign of Δz . Plugging these results back into (A3), we finally arrive at

$$\int_{\Gamma_z} d\Gamma' h(\mathbf{r}, \mathbf{r}') = \begin{cases} 1 & \text{if } Z > z \\ 0 & \text{if } Z < z \end{cases}. \quad (\text{A9})$$

Since the used form of the integral equation is valid for a normal vector pointing *into* the domain encircled by Γ , the integration contour should be closed *above* Γ_{sl} , so we have $Z > z$ [28]. Because the integral on the complete contour Γ is zero and there is no contribution by the contours $\Gamma_{\parallel 1}$ and $\Gamma_{\parallel 2}$ (which have finite length), due to the exponential decay of K_0 and K_1 for $x' \rightarrow \pm \infty$, we end up with

$$\int_{\Gamma_{sl}} d\Gamma' h(\mathbf{r}, \mathbf{r}') = -1. \quad (\text{A10})$$

Equation (2.9) is then immediately obtained by transforming to reduced variables and integrating out the contribution of the δ function.

APPENDIX B: A CONSEQUENCE OF GLOBAL MASS CONSERVATION

To investigate the consequences of mass conservation in the bulk we start from the most general form of the continuity equation which, in the frame moving with the interface, reads

$$\frac{\partial c}{\partial t} - V \frac{\partial c}{\partial z} = -\nabla \cdot \mathbf{j}_c. \quad (\text{B1})$$

\mathbf{j}_c is the mass current. In the liquid, where $\mathbf{j}_c = -D\nabla c$, this equation reduces to Eq. (2.1); at the liquid-solid boundary, one can derive Eq. (2.4) from it.

We now integrate Eq. (B1) over the domain Ω_0 delimited by the contour $\Gamma_0 = \Gamma_\alpha + \Gamma_\beta + \Gamma_{\parallel 1} + \Gamma_\infty + \Gamma_{\parallel 2}$ which is depicted in Fig. 17 and whose bottom pieces Γ_α and Γ_β lie inside the solid. Since we consider stationary solutions, $\partial c / \partial t$ equals zero. The remaining time-

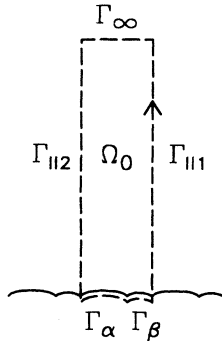


FIG. 17. Integration contour used to relate c_∞ to the concentrations $c_{s\alpha}$ and $c_{s\beta}$ in the solid.

independent integrals can be transformed into contour integrals (\mathbf{e}_z denotes the unit vector in z direction):

$$\begin{aligned} \int_{\Omega_0} d\Omega \frac{\partial c}{\partial z} &= \int_{\Omega_0} d\Omega \mathbf{e}_z \cdot \nabla c = - \int_{\Gamma_0} d\Gamma n_z c, \\ \int_{\Omega_0} d\Omega \nabla \cdot \mathbf{j}_c &= - \int_{\Gamma_0} d\Gamma \mathbf{n} \cdot \mathbf{j}_c. \end{aligned} \quad (\text{B2})$$

The contributions to the second integral from $\Gamma_{\parallel 1}$ and $\Gamma_{\parallel 2}$ cancel each other and, because of $\mathbf{j}_c = 0$ in the solid as well as at infinity, this integral vanishes altogether (there is no net flux out of the periodicity volume).

As to the first integral, we have $dx = n_z d\Gamma$ on Γ_α and Γ_β , $dx = -n_z d\Gamma$ on Γ_∞ , and $n_z = 0$ on the remaining pieces of Γ_0 . Hence, we immediately obtain (setting the coordinate of the triple point between Γ_α and Γ_β equal to $\eta\lambda$)

$$\begin{aligned} c_\infty &= \frac{1}{\lambda} \left[\int_0^{\eta\lambda} dx c_{s\alpha}(x, \zeta(x)) + \int_{\eta\lambda}^\lambda dx c_{s\beta}(x, \zeta(x)) \right] \\ &= \eta \langle c_{s\alpha} \rangle + (1-\eta) \langle c_{s\beta} \rangle, \end{aligned} \quad (\text{B3})$$

where $c_{s\alpha}$ and $c_{s\beta}$ stand for the concentrations in the α and β phases, respectively.

Returning to reduced lengths in units of λ , we can write

$$\begin{aligned} c_\infty - c_e &= \int_0^\eta dx (c_{s\alpha} - c_\alpha) + \int_\eta^1 dx (c_{s\beta} - c_\beta) \\ &\quad - c_e + \eta c_\alpha + (1-\eta) c_\beta, \end{aligned} \quad (\text{B4})$$

which on division by Δc becomes

$$u_\infty = \int_0^\eta dx u_{s\alpha} + \int_\eta^1 dx u_{s\beta} - \eta\delta + (1-\eta)(1-\delta), \quad (\text{B5})$$

where we have defined $u_{si} = (c_{si} - c_i) / \Delta c$ ($i = \alpha, \beta$). An immediate consequence of this definition is $u_{si} = k_i u(x, \zeta(x))$, which leads to

$$\begin{aligned} u_\infty + \delta + \eta - 1 &= k_\alpha \int_0^\eta dx u(x, \zeta(x)) + k_\beta \int_\eta^1 dx u(x, \zeta(x)) \\ &= -P \int_0^1 dx \epsilon(x) k(x) \\ &\quad \times [\chi \zeta(x) + \psi(x) \sigma \kappa(x)]; \end{aligned} \quad (\text{B6})$$

the definitions of $\epsilon(x)$, $k(x)$, χ , σ , and $\psi(x)$ have been given in Sec. VI. Equation (B6), which is identical to Eq. (6.28), is the desired result, showing that $(u_\infty + \delta + \eta - 1) / P$ does not diverge as $1/P$ but is of order 1.

APPENDIX C: CONVERGENCE CONSIDERATIONS

To see the convergence of I_{20} we may use the following theorem [29]: Given two integrable functions $h(t)$ and $g(t)$, if $h(t)$ is monotonic for $t \geq a$ and $\lim_{t \rightarrow \infty} h(t) = 0$ and if furthermore $\int_a^t du g(u)$ is bounded $\forall t \geq a$ then $\int_a^\infty dt g(t) h(t)$ exists, i.e., is convergent.

Substituting $y = x - x'$ for the integration variable in I_{20} , we can set, in the most slowly decaying term of the integral (whose convergence decides the convergence of the whole integral), $h(y) = y / \rho^2$, which behaves as $1/y$ for $y \gg x$ and hence becomes monotonic beyond some sufficiently large value $y = y_0$. We then have to prove

that the remaining factor $g_0(y) = (1/2\pi)\xi_y \bar{u}(x - y)$ has a bounded integral on arbitrary finite intervals. $\bar{u}(x)$ has been defined in Eq. (6.2). Now, ξ is a periodic function that is *even* with respect to the symmetry axes of the α and β phases due to the axisymmetry of the solutions considered here. Furthermore, \bar{u} is a function of ξ and its first and second derivatives, with the first ones appearing only in even powers; therefore, \bar{u} is also even. However, ξ_y is odd, being the first derivative of an even function. As a consequence, the total function g_0 is *odd* with respect to the symmetry axes of the phases. Hence, its integral over one period vanishes, and its integral on any interval $[y_0, y_1]$ remains bounded for arbitrarily large y_1 . This shows that $\int_{y_0}^{\infty} dt g_0(t)h(t)$ exists. Clearly, an analogous argument can be used to show convergence at the lower integration bound of I_{20} and hence, the convergence of the integral is proved.

In order to actually perform the limit $P \rightarrow 0$ we should like to have, however, *uniform* convergence of the integral I_2 on some P interval containing zero. To see this in detail, we first decompose the integral in three parts:

$$I_2 = I_{2a} + I_{2b} + I_{2c}, \tag{C1}$$

$$I_{2a} = \frac{1}{2\pi} \left[\int_{-\infty}^{-R_1} + \int_{R_2}^{\infty} \right] dy e^{-P\Delta\xi} \frac{\Delta\xi}{\rho} K_1(P\rho) P\bar{u}(x - y), \tag{C2}$$

$$I_{2b} = \frac{1}{2\pi} \left[\int_{-\infty}^{-R_1} + \int_{R_2}^{\infty} \right] dy e^{-P\Delta\xi} \frac{y\xi_y}{\rho} K_1(P\rho) P\bar{u}(x - y), \tag{C3}$$

$$I_{2c} = \frac{1}{2\pi} \int_{-R_1}^{R_2} dy e^{-P\Delta\xi} \left[\frac{\Delta\xi}{\rho} + \frac{y\xi_y}{\rho} \right] K_1(P\rho) P\bar{u}(x - y). \tag{C4}$$

It is understood that $\Delta\xi$ and ξ are both functions of the argument $x - y$, while $\rho = (y^2 + \Delta\xi^2)^{1/2}$. The numbers R_1 and R_2 are arbitrary positive numbers at the moment, the

$$I_{2a} + I_{2b} = \left[\int_{-\infty}^{-R_1} + \int_{R_2}^{\infty} \right] dy \left[F_P(y) \int_0^{\infty} dt \frac{\cos P\rho t}{(t^2 + 1)^{3/2}} - G_P(y) \left[\int_0^{\infty} dt \frac{\cos P\rho t}{(t^2 + 1)^{3/2}} - 3 \frac{y^2 - y\Delta\xi\xi_y}{\rho^2} \int_0^{\infty} dt \frac{\cos P\rho t}{(t^2 + 1)^{5/2}} \right] \right] \frac{1}{\rho^2}. \tag{C9}$$

It is clear that the integrals of the cosine terms are bounded by $\int_0^{\infty} dt (t^2 + 1)^{-3/2}$ ($=1$) and $\int_0^{\infty} dt (t^2 + 1)^{-5/2}$, respectively. Furthermore, F_P and G_P are bounded functions, whose dependence on P is continuous. Therefore, the expression in brackets, let us call it $I_P(y)$, is a bounded function of y for P in some interval $[0, P_0]$ with lower and upper bounds m and M , which can be chosen *independent* of P . Hence, we can, for any $\epsilon > 0$, choose (a large enough) R_2 such that

$$\left| \int_{R_2}^{\infty} dy I_P(y) \frac{1}{\rho^2} \right| \leq \max(|m|, |M|) \int_{R_2}^{\infty} dy \frac{1}{\rho^2} < \epsilon, \tag{C10}$$

only requirement being that $0 \in (-R_1, R_2)$ —otherwise the integrals I_{2a} and I_{2b} would each diverge at $y=0$. (Their sum is convergent.) Cutting out the middle part of integrals that originally extended from $-\infty$ to ∞ will also prove useful later when an integration by parts must be performed to generate an additional power of $1/\rho$.

The most convenient approach we have found is to use the following integral representation for K_1 :

$$K_1(P\rho) = \frac{\rho}{P} \int_0^{\infty} dt \frac{\cos Pt}{(t^2 + \rho^2)^{3/2}} \tag{C5}$$

(No. 8.432,5 in Ref. [25]). Inserting this in (C2) and (C3) we have, introducing

$$F_P(y) = (1/2\pi) e^{-P\Delta\xi} \Delta\xi \bar{u}(x - y)$$

and

$$g_P(y) = (1/2\pi) e^{-P\Delta\xi} \xi_y \bar{u}(x - y), \tag{C6}$$

$$I_{2a} = \left[\int_{-\infty}^{-R_1} + \int_{R_2}^{\infty} \right] dy F_P(y) \int_0^{\infty} dt \frac{\cos Pt}{(t^2 + \rho^2)^{3/2}},$$

$$I_{2b} = \left[\int_{-\infty}^{-R_1} + \int_{R_2}^{\infty} \right] dy g_P(y) y \int_0^{\infty} dt \frac{\cos Pt}{(t^2 + \rho^2)^{3/2}}. \tag{C7}$$

In this form of the equations, most of the P dependence has been shifted into the cosine terms. Setting $G_P(y) \equiv \int_{-R_1}^y dt g_P(t)$ for $y < -R_1$ and $G_P(y) \equiv \int_{R_2}^y dt g_P(t)$ for $y > R_2$, we perform an integration by parts on the second integral which yields

$$I_{2b} = - \left[\int_{-\infty}^{-R_1} + \int_{R_2}^{\infty} \right] dy G_P(y) \times \left[\int_0^{\infty} dt \frac{\cos Pt}{(t^2 + \rho^2)^{3/2}} - 3(y^2 - y\Delta\xi\xi_y) \int_0^{\infty} dt \frac{\cos Pt}{(t^2 + \rho^2)^{5/2}} \right]. \tag{C8}$$

Now we can substitute $t \rightarrow \rho t$ and arrive at

and this choice is independent of P . The same holds, of course, for R_1 and the integral extending from $-\infty$ to $-R_1$. This proves the uniform convergence of I_2 , because the middle part I_{2c} , having finite (P independent) integration bounds, is a continuous function of P . From uniform convergence it follows that I_2 is a continuous function of P , too, and therefore, $\lim_{P \rightarrow 0} I_2(P) = I_{20}$. This finishes our consideration of I_2 .

For the integral $I_1 = I_{1a} + I_{1b} + I_{1c}$, we have evaluated the last two terms in Sec. VI by explicit integration of Fourier series. The uniform convergence of I_{1a} can be proved by use of the representation (No. 8.432,5 in Ref. [25])

$$K_0(xz) = \int_0^\infty dt \frac{\cos xt}{(t^2+z^2)^{1/2}}, \quad (\text{C11})$$

with $x = P$ and $z = \rho$, $z = |\Delta x|$, respectively. Then, we have

$$\begin{aligned} K_0(P\rho) - K_0(P|\Delta x|) &= \int_0^\infty dt \cos Pt \left[\frac{1}{(t^2+\rho^2)^{1/2}} - \frac{1}{(t^2+\Delta x^2)^{1/2}} \right] \\ &= - \int_0^\infty dt \cos Pt \frac{\Delta x^2}{(t^2+\rho^2)(t^2+\Delta x^2)^{1/2} + (t^2+\Delta x^2)(t^2+\rho^2)^{1/2}} \\ &= - \frac{\Delta x^2}{\rho^2} \int_0^\infty dt \frac{\cos P\rho t}{(t^2+1)(t^2+\Delta x^2/\rho^2)^{1/2} + (t^2+\Delta x^2/\rho^2)\sqrt{t^2+1}}. \end{aligned} \quad (\text{C12})$$

Inserting this into the definition of I_{1a} [see Eq. (6.13)] and again splitting the integration into three parts,

$$\int_{-\infty}^\infty \dots = \int_{-\infty}^{-R_1} \dots + \int_{-R_1}^{R_2} \dots + \int_{R_2}^\infty \dots,$$

we can use the fact that the above expression is bounded by a constant times $1/\rho^2$ in the two integrals on infinite intervals to demonstrate the uniform convergence of I_{1a} .

-
- [1] J. S. Langer, in *Proceedings of the Les Houches Summer School, Session 46*, edited by J. Souletie, J. Vannimenus, and R. Stora (Elsevier, Amsterdam, 1987).
- [2] W. W. Mullins and R. F. Sekerka, *J. Appl. Phys.* **35**, 444 (1964).
- [3] For a recent review, see H. Müller-Krumbhaar and W. Kurz, in *Materials Science and Technology*, edited by R. W. Cahn, P. Haasen, and E. J. Kramer (VCH Verlagsgesellschaft, Weinheim, 1991), p. 553.
- [4] J.-M. Flesselles, A. J. Simon, and A. J. Libchaber, *Adv. Phys.* **40**, 1 (1991).
- [5] Note that eutectics can be formed for alloys that are far away from the eutectic composition. They may exist in a rather wide region, in the $\alpha + \beta$ coexistence domain. This region is generally referred to as the coupled zone (see Ref. [13]).
- [6] J. D. Hunt and K. A. Jackson, *Trans. Metall. Soc. AIME* **236**, 843 (1966).
- [7] V. Seetharaman and R. Trivedi, *Metall. Trans. A* **19**, 2955 (1988).
- [8] K. A. Jackson and J. D. Hunt, *Trans. Metall. Soc. AIME* **236**, 1129 (1966).
- [9] R. Trivedi, J. T. Mason, and W. Kurz, *Acta. Metall. A* **19**, 2964 (1988).
- [10] K. Brattkus, B. Caroli, C. Caroli, and B. Roulet, *J. Phys. (Paris)* **51**, 1847 (1990).
- [11] K. Kassner and C. Misbah, *Phys. Rev. Lett.* **65**, 1458 (1990); **66**, 522(E) (1991).
- [12] K. Kassner and C. Misbah, *Phys. Rev. Lett.* **66**, 445 (1991).
- [13] For a review, see G. Lesoult, *Ann. Chim. Fr.* **5**, 154 (1980).
- [14] C. Misbah, H. Müller-Krumbhaar, Y. Saito, and D. Temkin, in *Nonlinear Phenomena Related to Growth and Form*, edited by M. Ben Amar, P. Tabeling, and P. Pelcé (Plenum, New York, in press).
- [15] We should mention that, strictly speaking, the latent heats that enter the definition of the capillary lengths d_0^i are not exactly those of the α -liquid and β -liquid transitions, but effective quantities. The derivation given in Ref. [30] for a quasiazeotrope may serve as a guide for a check of this remark. We see there that, only because the concentrations of the solid and liquid phases are equal at the azeotropic point (which is not the case for eutectics), the effective heat of transition reduces to the latent heat.
- [16] Note that Eqs. (2.4) are in fact a simplification of the exact mass-conservation equations for a nondilute system. Indeed, the terms in the square brackets must be understood as $(c_l - c_{si})$, $i = \alpha, \beta$. Thermodynamic equilibrium at the front imposes that (see Ref. [30]) $(c_{si} - c_l) = k_i(c_l - c_e) + d_0^i \kappa$, where κ is the front curvature. The capillary length d_0^i , which vanishes for dilute alloys, turns out to be negligible for eutectics with small temperature gaps ($m_i \Delta c_i$). This is the case for the $\text{CBr}_4\text{-C}_2\text{Cl}_6$ eutectic in which we are interested here. We should, however, keep in mind that there are some eutectics for which d_0^i is not small, especially due to a large temperature gap (e.g., Pb-Sn).
- [17] B. Caroli, C. Caroli, B. Roulet, and J. S. Langer, *Phys. Rev. A* **33**, 442 (1986).
- [18] Y. Saito, G. Goldbeck-Wood, and H. Müller-Krumbhaar, *Phys. Rev. A* **38**, 2148 (1988).
- [19] V. Datye and J. S. Langer, *Phys. Rev. B* **24**, 4155 (1981).
- [20] C. A. Brebbia, *The Boundary Element Method for Engineers* (Penetech, London, 1978).
- [21] *Handbook of Mathematical Functions*, edited by M. Abramowitz and I. A. Stegun (Dover, New York, 1972).
- [22] This means that lengths are measured in multiples of l_T and times in multiples of $\tau \equiv l_T^2/D$. We give an example of the mapping to physical units. Typical values for the parameters in a directional solidification experiment on $\text{CBr}_4\text{-C}_2\text{Cl}_6$ are $m_\alpha = 1.5$ K/wt. %, $\Delta c = 15$ wt. %, $G = 60$ K/cm, and $D = 10^{-5}$ cm²/s. Therefore, $l_T^2 = 0.375$ cm and the time unit is $\tau = 14062.5$ s. The other quantities are calculated to be $\lambda_{\min} = 41.6$ μm , $V = 1.07$ $\mu\text{m/s}$, and $d_0^{\alpha/\beta} = 37.5$ nm.
- [23] L. H. Ungar and R. A. Brown, *Phys. Rev. B* **29**, 1367 (1984); **30**, 3993 (1984); **31**, 5923 (1985); **31**, 5931 (1985).
- [24] This is a divergence in the strict mathematical sense. If

the integral is reinterpreted as a principal value integral, i.e., $\int_{-\infty}^{\infty} dx' \cdots \rightarrow \lim_{R \rightarrow \infty} \int_{-R}^R dx' \cdots$, it is convergent for arbitrary profiles, because the diverging contributions, by the symmetric part of $\zeta_{x'}$, from the lower and upper integration bounds cancel each other. For axisymmetric profiles, $\zeta_{x'}$ is antisymmetric, and the integral converges in the ordinary sense.

- [25] I. S. Gradshteyn and I. M. Ryzhik, *Table of Integrals, Series, and Products* (Academic, Orlando, 1980).
- [26] In the similarity equation given in Ref. [12], the terms stemming from b_0 and $d_0(P)$ were neglected, because their integrand was $O(P \ln P)$. The aforementioned cancellation shows that for consistency they should be taken into account.
- [27] K. Brattkus and C. Misbah, *Phys. Rev. Lett.* **64**, 1935 (1990).
- [28] Contrary to what the notation suggests, $h(\mathbf{r}, \mathbf{r}')$ is not a function of \mathbf{r} and \mathbf{r}' alone [which $g(\mathbf{r}, \mathbf{r}')$ is]. To calculate $h(\mathbf{r}, \mathbf{r}')$, one must, in addition to its arguments, know the piece of boundary contour that goes through \mathbf{r}' (and its orientation), in order to evaluate the normal direction. If this is properly taken into account, one can of course derive the sum rule as well by closing the contour below Γ_{sl} .
- [29] *Mathematik-Handbuch für Technik und Wissenschaft*, edited by J. Dreszer (Deutsch, Zürich, 1975), p. 239.
- [30] C. Misbah, *J. Phys. (Paris)* **47**, 1077 (1986).